# Dependence of Phase Diagram of BSCCO on Disorder and Anisotropy

*Ph.D. thesis*

submitted by: Tal Verdene
Supervisor: Prof. Eli Zeldov

March 24, 2008

# CONTENTS

# 1. ABSTRACT

In this work we studied the $B-T$ phase diagram of vortex matter in high-$T_c$ and low-$T_c$ type II superconductors. First and second order phase transitions of vortex matter in the layered high-$T_c$ superconductor $Bi_2Sr_2CaCu_2O_8$ were mapped using local magnetization measurements with micro Hall-sensor arrays. The equilibrium measurements down to $\sim$ 27K were obtained by utilization of the shaking method, in which an in-plane ac field is applied to relax vortices to their equilibrium configuration. Transport measurements were performed in order to study the dynamic behavior of vortex matter in the low-$T_c$ superconductor $NbSe_2$. Measurements of the self-field induced by ac current in the new superconductor $MgB_2$ were performed within the study of its edge and bulk related mechanisms.

We present thermodynamic evidence for new first-order - second-order - first-order behavior of the melting line in BSCCO samples irradiated with a low density of columnar defects. This unusual behavior is due to close competition between four different energy scales in the dilute columnar defects limit. As columnar defects are introduced, the melting transition initially alters its order from first to second at intermediate temperatures where correlated pinning has a dominant effect. At high and low temperatures the transition remains first-order despite the disordering potential of columnar defects. As the density of the columnar defects is increased, the second-order segment of the transition line expands both to the higher and lower temperatures. The observed nucleation and growth process of the second-order segment along the original first-order transition line clarifies the general process of transformation of phase transitions with increased disorder.

We found that disorder and thermal-fluctuations weaken relative to elasticity with increased oxygen doping, which shifts the first-order melting line towards higher fields. Disorder still gains relative dominance over thermal fluctuations, which concurrently shifts the maximum of the first-order line and its bisection with the second-order line towards higher temperatures.

We present evidence which suggest that the disordered metastable states near the peak effect of the critical current in $NbSe_2$ are enhanced by the presence of columnar defects. Whether this enhancement occurs predominantly at the edges of the sample and is linked to the edge contamination

mechanism or in the bulk of the sample remains an open question for future investigation.

# 2. ACKNOWLEDGEMENTS

I would like to thank my supervisor, Prof. Eli Zeldov, for his guidance and advice, Prof. Victor Steinberg for his support, Dr. Yuri Myasoedov for his assistance and patience, Dr. Michael Rappaport for his help in overcoming experimental obstacles, Yehonatan Segev for his help in producing various types of disordered samples, and my group members Sarah, Haim, Beena, Nurit, Yehonatan and Amit for their friendship and support.

# 3. INTRODUCTION

The interplay between different energy scales of a physical system can induce phase transitions and yield a rich phase diagram. In particular, in a clean system a melting transition results from the competition between elasticity and thermal fluctuations and is usually of a first order nature. The presence of a third competing scale due to strong disorder can suppress it to second order [1, 2] and lead to an even richer picture, the understanding of which is still limited.

Type II superconductors serve as excellent model systems for studying these phenomena. In their mixed phase, an applied external magnetic field penetrates the sample as quantized flux lines called vortices which interact repulsively with each other. The physical parameters of the vortex system can be changed quite easily. Their density can be changed by varying the magnitude of the external magnetic field. Point or correlated disorder can also be increased by irradiating the samples. In the layered high temperature superconductors the anisotropy, which determines the stiffness of the vortices and thus their susceptibility to the effect of thermal fluctuations and disorder can also be varied in a relatively easy manner. By varying their oxygen doping, the anisotropy along with the density of point disorder is varied.

Within this work we studied the interplay between some of these parameters in the vortex matter of high and low temperature superconductors. In section 7.1, in order to gain insight into the various competing mechanisms that determine the order of the melting transition and mold the phase diagram of the high temperature superconductor $Bi_2Sr_2CaCu_2O_8$, we introduced an additional control parameter in the form of a variable weak correlated disorder. As a result, an exceptionally intricate behavior emerged where the initially first-order melting transition of the vortex matter exhibits a rare three-section first- second- and first-order behavior and even seems to undergo a four section first- second- first- and second-order sequence.

In section 7.2 we studied the oxygen doping dependence of the equilibrium first-order melting and second-order glass transition of vortices in $Bi_2Sr_2CaCu_2O_8$. Doping affects both anisotropy and disorder. We showed that the second order line scales with material anisotropy even where the first order line does not. In addition, we show that effective disorder weakens

with doping, but gains relative dominance over thermal fluctuations.

Section 7.3 of this work is dedicated to the study of the effect of weak correlated disorder on the dynamic behavior of vortices in the low temperature superconductor $NbSe_2$ in the vicinity of the peak effect of the critical current. Correlated disorder seems to enhance metastable disordered states of vortices that may originate from the bulk of the sample and from edge contamination. Our understanding of these intriguing results is yet incomplete and calls for additional experiments.

Section 7.4 is dedicated to the study of the bulk dominated and surface dominated regimes in the phase diagram of the newly discovered superconductor $MgB_2$. Within this work we explored the possibility that a crossover between two such regimes may explain the two staged resistive transition which was observed in $MgB_2$ and whose origin is unresolved.

# 4. SCIENTIFIC BACKGROUND

## *4.1 Ginzburg - Landau Theory*

The Ginzburg-Landau theory [3] does not purport to explain the microscopic mechanisms which give rise to superconductivity. Instead, it examines the macroscopic properties of a superconductor with the aid of general thermodynamic arguments. Based on Landau's previously-established theory of second-order phase transitions, Landau and Ginzburg argued that the free energy F of a superconductor near the superconducting transition can be expanded in powers of a complex order parameter $\psi(\mathbf{r})$. The free energy density has the form

$$F = F_{n0} + \alpha|\psi|^2 + \frac{\beta}{2}|\psi|^4 + \frac{1}{4m}\left|\left(-i\hbar\nabla - \frac{2e}{c}\mathbf{A}\right)\psi\right|^2 + \frac{\mathbf{H}^2}{8\pi} \tag{4.1}$$

where $F_n$ is the free energy density in the normal phase at zero magnetic field, $\alpha$ and $\beta$ are parameters that depend on temperature and material, $\mathbf{A}$ is the electromagnetic vector potential, and $\mathbf{H}$ is the external magnetic field. By minimizing the free energy with respect to fluctuations in the order parameter and the vector potential, one arrives at the Ginzburg-Landau equations

$$\alpha|\psi| + \beta|\psi|^2\psi + \frac{1}{4m}\left(-i\hbar\nabla - \frac{2e}{c}\mathbf{A}\right)^2\psi = 0 \tag{4.2}$$

$$\mathbf{J} = \frac{e\hbar}{2mi}\left(\psi^*\nabla\psi - \psi\nabla\psi^*\right) - \frac{2e^2}{mc}\psi^*\psi \tag{4.3}$$

where $\mathbf{J}$ denotes the electrical current density. The first equation determines the order parameter $\psi$. The second equation then provides the superconducting current. These equations have two homogeneous solutions:

1. $\psi = 0$ and $curl\mathbf{A} = \mathbf{H}$, this solution describes the normal state.
2. $\psi = \psi_0 \equiv (-\alpha/\beta)^{\frac{1}{2}}$ and $\mathbf{A} = 0$, this solution describes the superconductor in the Meissner state.

The Ginzburg-Landau equations produce many valid results. Amongst these is its prediction of the existence of two characteristic lengths in a superconductor. The first is a coherence length $\xi$, given by

$$\xi(T) = \sqrt{\frac{\hbar^2}{2m|\alpha(T)|}} \tag{4.4}$$

which describes the scale of spatial variations of the order parameter. The second is the penetration depth $\lambda$, given by

$$\lambda = \sqrt{\frac{mc^2}{16\pi e^2 \psi_0^2}} \tag{4.5}$$

The penetration depth describes the depth to which an external magnetic field can penetrate the superconductor.

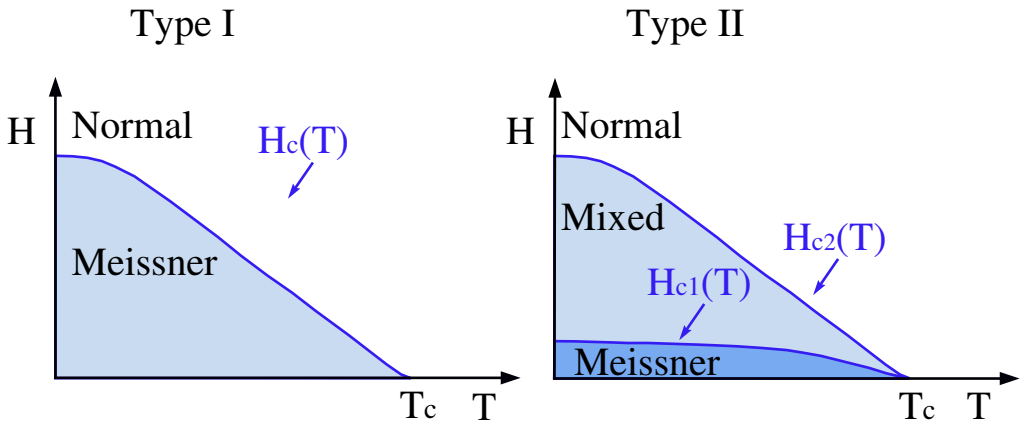


*Fig. 4.1:* A schematic phase diagram of type $I$ and type II superconductors

The ratio $\kappa = \lambda/\xi$ is known as the Ginzburg-Landau Parameter. The magnetic behavior of superconductors is characterized according to the value of their Ginzburg-Landau Parameter, $\kappa$. In substances with $\kappa > 1/\sqrt{2}$, the formation of normal-superconducting boundaries is energetically favored. These substances form a group of superconductors referred to as type II superconductors. Substances with $\kappa < 1/\sqrt{2}$ are referred to as type $I$ superconductors, in which the formation of such normal-superconducting boundaries is energetically unfavored. The phase diagram of a type $I$ superconductor is comprised of two homogeneous phases, the normal and the Meissner phase, separated by the $H_c(T)$ transition line (see phase diagram in figure 4.1).

Below this line, exists the Meissner phase in which the superconductor displays perfect diamagnetism expelling any magnetic field. At high magnetic fields, above the transition line, the material is in its normal state and magnetic field penetrates completely. A type II superconductor has an additional phase, the mixed phase, in which field enters the sample in form of flux tubes - vortices (see phase diagram in figure 4.1).

A special case of the Ginzburg-Landau theory is its form used for anisotropic material such as the layered high temperature superconductors. Their layered structure renders also $\xi$ and $\lambda$ anisotropic

$$\epsilon \equiv \left(\frac{m_{ab}}{m_c}\right)^{\frac{1}{2}} = \frac{\lambda_{ab}}{\lambda_c} = \frac{\xi_c}{\xi_{ab}} \leq 1 \tag{4.6}$$

where $m_{ab}$ and $m_c$ are the effective masses within and perpendicular to the superconducting a-b planes. If the interlayer coupling is weak, then $m_c \gg m_{ab}$. This quantity differs for different materials, but can also be varied by changing the oxygen content in the copper-oxide substances.

The anisotropic Ginzburg-Landau free energy density is:

$$F^{AGL} = F_{n0} + \alpha|\psi|^2 + \frac{\beta}{2}|\psi|^4 + \sum_{\mu=x,y,z} \frac{1}{4m_\mu} \left|\left(-i\hbar\nabla_\mu - \frac{2e}{c}A_\mu\right)\psi\right|^2 + \frac{\mathbf{H}^2}{8\pi} \tag{4.7}$$

with $m_x = m_y = m_{ab}$, $m_z = m_c$.

It was shown [4] that in the limit $B \gg H_{c1}$ a simple scaling scheme can reduce the anisotropic Ginzburg-Landau expansion back to the Ginzburg-Landau expansion, yielding a scaling rule that produces any anisotropic quantity from its isotropic counterpart.

## 4.2 The Mixed Phase of Type II Superconductors

As predicted by Abrikosov in 1956 based on the Ginzburg-Landau theory, in the mixed phase when the external field is in the range $H_{c1} < H < H_{c2}$ it penetrates the sample as vortices. Every vortex has a quantum unit of flux $\phi_0 = \frac{hc}{2e}$ associated with it. It has a normal core whose radius is the coherence length, $\xi$. Around it there are circulating currents that define its magnetic profile. In the center, the magnetic field has its highest value, which decays exponentially over a length $\lambda$ (See figure 4.2 for the structure of an Abrikosov vortex).

According to Abrikosov, these vortices form a perfect (hexagonal) lattice due to their repulsive interaction. In real materials, however, a lattice phase occurs in only a small fraction of the phase space, owing to additional factors such as temperature and material disorder.

The Abrikosov lattice was first observed a decade after it was theoretically predicted using the Bitter decoration method [5]. This observation was followed by numerous supporting measurements, utilizing various experimental techniques such as neutron scattering [6, 7], electron microscopy [8], electron holography [9], scanning-tunnelling microscopy [10], Hall probe microscopy [11] and magneto-optics [12].

Within the mixed phase, the partial penetration of flux renders intricate transport properties. In the presence of transport current, vortices are deflected due to the Lorenz force, given by $F = \mathbf{J} \times \phi_{\mathbf{0}}$, where $\mathbf{J}$ is the transport current density and $\phi_{\mathbf{0}}$ is a vector of magnitude $\frac{hc}{2e}$ directed along the flux line. The motion of vortices with the action of viscous drag results in finite dissipation. In real materials, however, inhomogeneities act as local traps which restrain the motion of vortices (pinning). Then, perfect conductivity is retained up to a critical current $I_c(H, T)$, which is defined as the smallest current such that the Lorentz force exceeds the pinning force.

Pinning centers can also be introduced to the sample artificially. Irradiation by electrons or protons produce point like pinning centers. A more effective means of pinning the vortices is achieved with elongated pinning

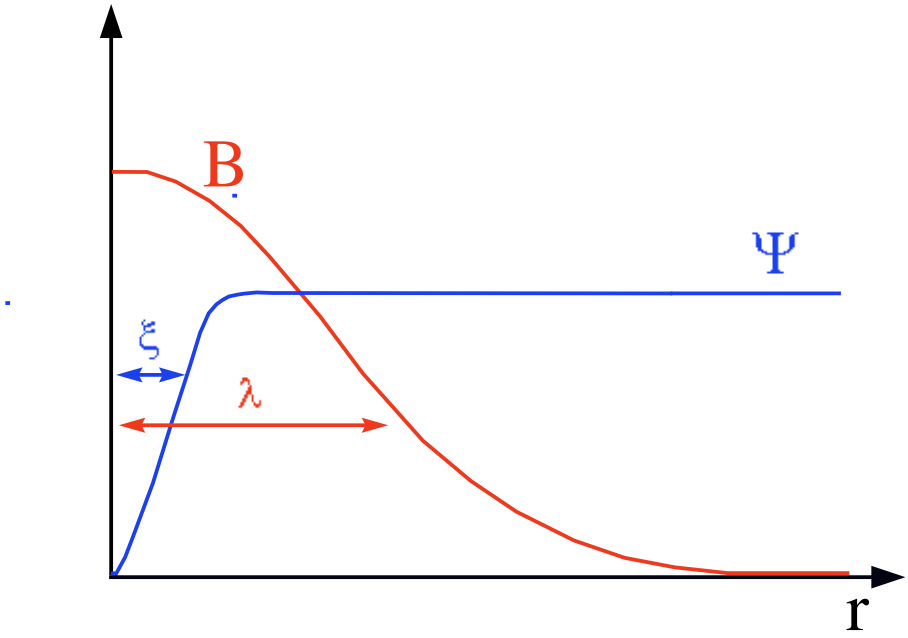


*Fig. 4.2:* The structure of an Abrikosov vortex with a normal core of radius $\xi$ and a magnetic field decaying radially over $\lambda$

centers: columnar defects. These defects can be introduced to the sample by bombardment with heavy ions. The effect of dilute columnar defects on the thermodynamic behavior of the high temperature superconductor $Bi_2Sr_2CaCu_2O_8$ (BSCCO) is studied in section 7.1 of this work. Section 7.3 is dedicated to their effect on the dynamic behavior of the low temperature superconductor $NbSe_2$ near the region of the peak effect.

### 4.2.1 Vortex Matter in High Temperature Superconductors - $Bi_2Sr_2CaCu_2O_8$

In 1986 Müller and Bednortz discovered the first member of a new group of superconductors; the high-$T_c$ superconductors. Members of this family have high critical temperatures, sometimes well above the liquifying temperature of Nitrogen. This feature makes these substances particularly attractive for practical applications. The high temperature superconductors have a small coherence length, $\xi$ and a large penetration depth $\lambda$, resulting in large values of the Ginzburg-Landau parameter, $\kappa$, which makes them extreme type II. Common to all members of this group is their layered structure. They consist of superconducting Copper-Oxide planes separated by metallic or insulating materials which serve as charge reservoirs. This structure causes them to be also highly anisotropic in their magnetic behavior.

In their mixed state, as in conventional superconductors, a field penetrates the sample in form of vortices. Yet the structure of the individual vortices as well as that of the vortex lattice is quite different. Unlike the continuous Abrikosov vortices, a transverse magnetic field penetrates a layered superconductor as vortices that behave more like a stack of "pancake" vortices in each superconducting layer with only a weak correlation between them. An in-plane field penetrates these superconductors as "Josephson" vortices whose cores reside in between the superconducting layers. Pancake vortices that reside in the same layer interact repulsively with each other, in similarity to Abrikosov vortices. Pancake vortices in adjacent layers, on the other hand, are weakly coupled by magnetic and Josephson interactions.

The highly anisotropic magnetic behavior of high temperature superconductors, which is manifested by the softened stack structure of the vortices, combined with their high operating temperatures results in enhanced thermal fluctuations. This is manifested by a very high Ginzburg number $Gi = (T_c/\epsilon_0\xi_c)^2/8$ [13, 14] which is particularly high in BSCCO ($Gi \approx 1$).

As a result of the interplay between the repulsive interaction between the vortices and thermal fluctuations, the ordered lattice which was predicted by Abrikosov to occupy the entire mixed state undergoes a first order melting transition into a disordered vortex state [15, 16]. In high temperature

superconductors the disordered phase prevails in most of the mixed phase (for a schematic H-T phase diagram of a clean type II superconductor see figure 4.3). This transition was predicted theoretically [15] and measured by numerous experimental methods, among them transport [17, 18], magnetization [16, 19], *ac* susceptibility [20], calorimetric [21], neutron diffraction [22] and muon spin rotation [23].

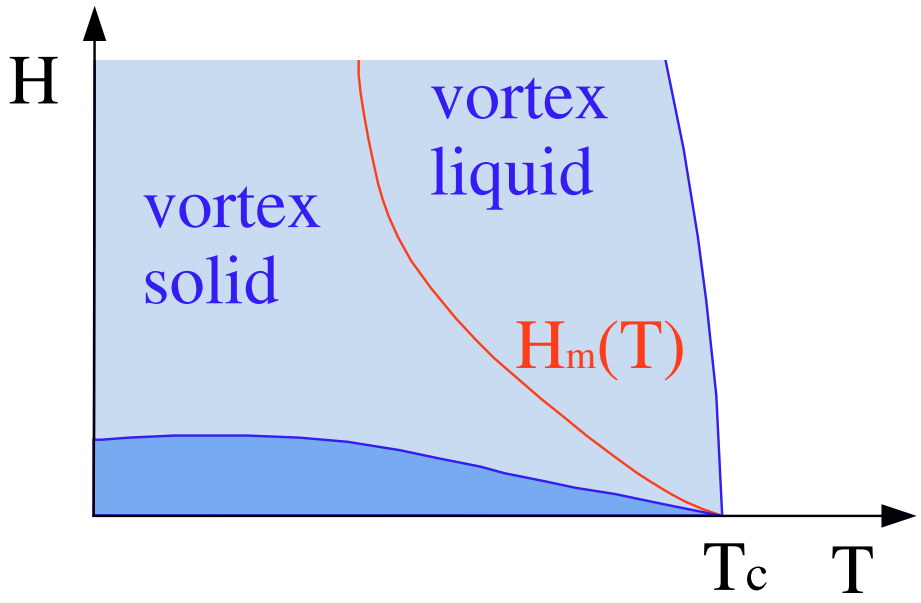


*Fig. 4.3:* Schematic H-T phase diagram of clean type II superconductors. Thermal fluctuations drive a first order melting transition $H_m(T)$ from the ordered vortex solid phase into a disordered vortex liquid phase.

In addition to thermal fluctuations and elasticity, other factors affect the behavior of vortex matter within the mixed state. In real samples point material disorder is always present. These randomly distributed imperfections serve as potential wells which can trap vortices and prevent them from acquiring their equilibrium positions. It has been shown that the presence of point defects, even of infinitesimal concentration causes the perfectly ordered vortex lattice to lose its long range order [24, 25] and to be replaced by a quasi long range ordered Bragg glass phase [26, 27]. It is characterized

by logarithmically growing displacements on large distances [28] and an algebraically slow decay of positional correlations [27], which implies algebraically divergent Bragg peaks in the structure factor [26].

At low temperatures, calculations show that with the increase in the magnetic field the energetic gain from disorder grows faster than elasticity [29, 30, 31, 32, 33, 34]. This trend continues up to a critical value where dislocations become favorable and proliferate. As a result, a disorder driven first order transition occurs [35, 36, 37]. Upon this transition, the Bragg glass phase is transformed into an amorphous vortex glass phase. The potential wells of point defects can be smoothed by thermal fluctuations, making them effectively shallower [38]. Consequently, as the temperature is increased the transition is pushed to higher fields resulting in a positive slope of the melting line at low temperatures: the inverse melting.

In the mixed state of BSCCO, an additional transition line which is due to quenched disorder is believed to exist. An almost vertical second order glass transition [39, 40] apparently bisects the first order line separating between the glass phase and the depinned vortex liquid at high fields above the melting line and between the Bragg glass and possibly an ordered lattice at lower fields (for a schematic H-T phase diagram of type II superconductors in the presence of point disorder see figure 4.4)

As a result of the temperature dependence of the pinning affectivity, the phase diagram of high temperature superconductors consists of an additional line of dynamic nature: the irreversibility line. At low temperatures below this line, vortex matter is characterized by a hysteretic behavior, whereas above this line at high temperatures it is reversible.

Point disorder can also be introduced artificially. It has been shown [41] that enhanced point disorder destabilizes the quasi lattice Bragg phase and causes the maximum of the melting line to shift to lower fields and to higher temperatures.

More effective pinning can be achieved by introducing columnar defects to the sample. These defects are known to change the phase diagram entirely when at high densities $B_\phi \gg B_m(T)$, where $B_\phi = n_{cd}\phi_0$, $n_{cd}$ is the density of columnar defects, $\phi_0$ is the flux quantum, and $B_m(T)$ is the temperature-dependent melting field. Compared to the correlated pinning energy, the elastic energy of the vortices becomes negligible. This system can be mapped into the previously-studied problem of two dimensional Bosons on a random substrate [15, 42, 43]. According to this analysis, the ordered solid phase is replaced by a disordered Bose glass phase in which vortices are localized on columnar defects and a second order Bose glass transition emerges from the first order melting line [42, 44]. In addition, a Mott-insulator appears as a low-temperature line phase at the matching field $B_\phi$. At higher temperatures

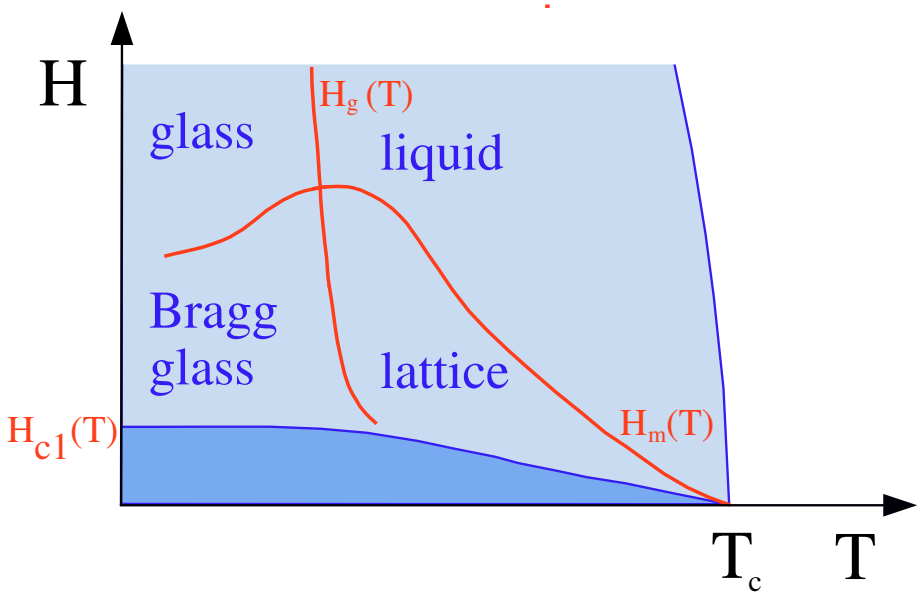


*Fig. 4.4:* Schematic H-T phase diagram of type II superconductors with point disorder. A first order melting transition $H_m(T)$ is temperature driven at high temperatures and disorder driven at low temperatures. A second order glass transition $H_g(T)$ separates between the low temperature pinned phases and the high temperature depinned phases.

the Mott-insulator line turns into a crossover line, above which interactions become relevant within the Bose-glass.

In section 7.1 of this work we concentrate on the dilute columnar defect limit in BSCCO, where vortices outnumber the columnar defects at most relevant fields. Remarkably, in this limit the energy due to correlated pinning is comparable to the other three energy scales: that of thermal energy, of elasticity and that due to point pinning. Consequently, the four relevant energy scales mold together a particularly complex $B-T$ phase diagram whose nature is not well-understood. Most theoretical studies [45, 46] and numerical simulations [47, 48] agree that at high temperatures the transition remains first order. At intermediate temperatures, where the phase transition occurs at fields that lie above the matching field, $B_m > B_\phi$, the majority of columnar defects are occupied by pinned vortices, and the remaining vortices

reside in between them. In this temperature range, the interstitial vortices are believed to undergo second order melting from nano-crystals below the transition to nano-droplets above it [45, 46, 47, 48, 49]. In the nano-crystal phase the interstitial vortices are believed to be arranged in an ordered lattice whereas in the nano-liquid phase they are melted into a liquid. At an even higher temperature, the vortices which were pinned on the columnar defects undergo a delocalization transition into a vortex liquid [50] (for a schematic

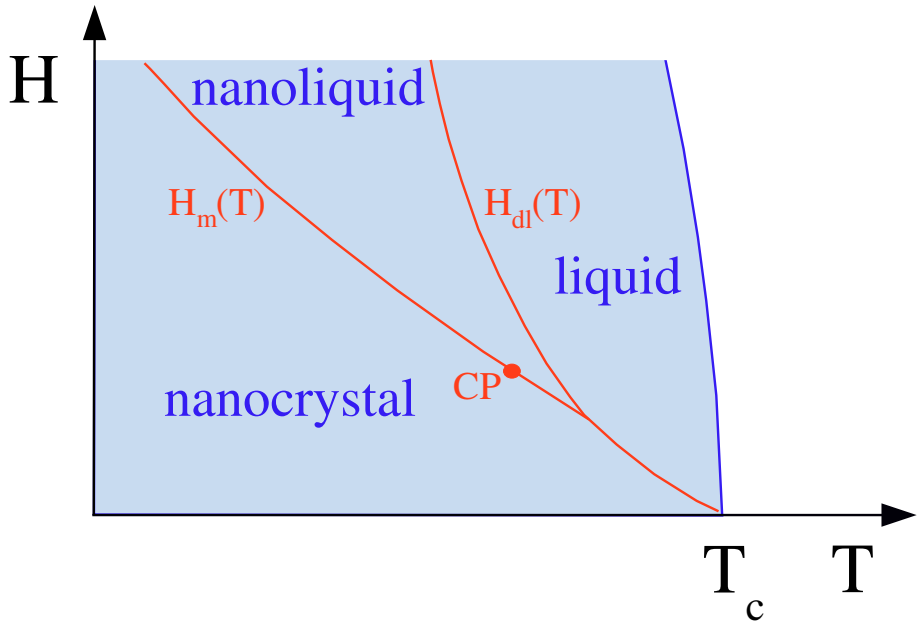


*Fig. 4.5:* Schematic phase diagram of BSCCO in presence of dilute columnar defects. Below the delocalization line $H_{dl}(T)$, the majority of columnar defects are occupied by pinned vortices, and the remaining vortices reside in between them forming ordered nanocrystals in the solid phase and nanodroplets in the liquid phase. The transition between these phases, $H_m(T)$, at high temperatures, above the critical point (CP), remains first-order, whereas at intermediate temperatures becomes second-order. Above $H_{dl}(T)$, vortices are delocalized and a homogeneous liquid phase resides.

H-T phase diagram see figure 4.5).

Experimentally, even a low density of columnar defects enhances hysteretic effects throughout most of the solid phase [51]. This is a major obstacle in mapping the true thermodynamic phase transitions of vortex matter. In lack of access to the thermodynamic behavior, past experimental studies have focused on dynamics [49, 51, 52]. They found that the high temperature FO transition line terminates at a critical point (CP) whose location depends on columnar defect density [49, 51, 52], in agreement with theory. At temperatures below the CP, however, these out-of-equilibrium studies could not evaluate the exact nature of the transition. Thus, a SO transition was premised to exist at all temperatures below the CP [45, 47, 48, 49, 51], though other theoretical scenarios were considered too [46]. This incomplete understanding of the dilute-pin-limit lead naturally to the assumption that as columnar defect density is increased, the SO nature of the transition spreads from low temperatures to higher ones with a shift of a single CP. The findings presented in 7.1, however, suggest a more complex behavior.

Disorder in high temperature superconductors can also be varied indirectly, along with the anisotropy, by changing their oxygen doping. As a result, the phase diagram of vortex matter is changed and the melting line shifts to higher fields with the increase in the oxygen doping [53, 54, 55]. The added oxygen molecules contribute charge carriers to the charge reservoir. Consequently, the correlation length perpendicular to the $CuO_2$ layers $\xi_c$ becomes larger and the coupling between superconducting layers increases, rendering a more isotropic behavior and stiffer pancake vortex stacks. A quantitative anisotropy scaling behavior for the high temperature part of the melting line has been established experimentally [53, 54, 56]. At low temperatures, however, the anisotropy scaling of the inverse melting and glass transition lines have not been studies in the past.

As stated above, in addition to the effect of the charge carriers donated by the oxygen molecules on the anisotropy, the increased concentration of oxygen ions is known to be closely linked to the pinning properties of the sample. Overdoping was shown to enhance the value of the critical current at low temperatures and high fields [57]. It was thus concluded that overdoped samples have a smaller concentration of material disorder and that it is the oxygen vacancies that serve as pinning centers [57]. A closer inspection of the effect of disorder and anisotropy on vortex matter behavior as the oxygen doping of BSCCO is varied in section 7.2 of this work suggests a more intricate interplay between the two. Within this work anisotropy rescaling was applied both to the full first order and to the second order transition lines. It shows that the second order line scales with material anisotropy even at temperatures where the first order line does not.

### 4.2.2 Vortex Matter in Low Temperature Superconductors - $NbSe_2$: The Peak Effect

In some high temperature superconductors and many low temperature ones, including $NbSe_2$, at fields close to $H_{c_2}$ an anomalous phenomenon was found. When the magnetic field is increased, a gradual and smooth increase in the critical current is observed before it vanishes at $H_{c_2}(T)$ [58, 59, 60, 61, 62]. This phenomenon is called the peak effect (PE). It is a result of a structural transition of the vortex matter [25, 63, 64, 65]. Below the peak region a quasi ordered phase is present. On approaching the peak region, the increased softening of the lattice causes a transition into a disordered vortex phase. In the low field ordered phase, there is almost no pinning and the critical current is low. In the high field disordered phase vortices can accommodate better to the pinning landscape and the critical current is high.

For a while, the smooth shape of the PE lead to the belief that the vortex matter gradually softens on approaching $H_{c_2}(T)$, but nowadays it is widely accepted that the transition is a disorder-driven first-order transition [66] similar to the disorder-driven inverse melting in high $T_c$ superconductors. In addition, it also has a reentrant behavior at low fields in which the peak effect also appears in dynamic measurements. So why doesn't the peak in the critical current look sharp as one would expect? It turns out that even below the transition, where the quasi ordered phase is energetically favorable, a disordered metastable phase can exist in the sample (see figure 4.6 for a schematic phase diagram). In the usual bar geometry, this metastability is injected through the edges of the sample due to a mechanism called edge contamination [67]. In close proximity to the transition, the lifetime of this metastable state is long. At fields farther from the transition, however, the energy difference between the equilibrium quasi ordered phase and the disordered metastability is larger, thus the lifetime of the metastable phase becomes shorter and the total critical current gradually decreases.

The quasi ordered phase is believed to be a Bragg glass phase [29, 31, 68], yet the exact nature of the disordered phase is still unknown. One suggestion is that it is an entangled liquid phase of vortices [69]. If so, it should be interesting to probe its behavior by introducing columnar defects. These defects are elongated in the c axis of the superconductor and may stretch the vortices and disentangle them, inducing order. Section 7.3 of this work is dedicated to the effect of dilute columnar defects on $NbSe_2$ in the vicinity of the peak effect.

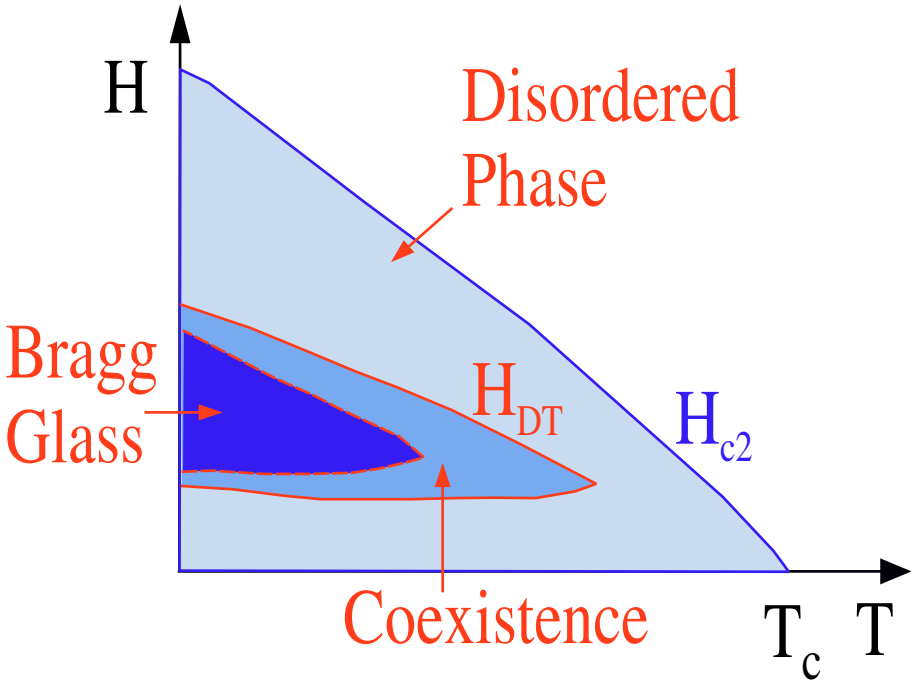


*Fig. 4.6:* Schematic H-T phase diagram of the low temperature superconductor $NbSe_2$, showing the disorder-driven first-order phase transition line $H_{DT}$ (with reentrant behavior) where the peak effect occurs in dynamic measurements. It shows the disordered phase, the ordered Bragg glass phase and a coexistence region where a stable ordered phase and metastable disordered states coexist.

### *4.2.3 Superconductivity in $MgB_2$*

Superconductivity in $MgB_2$ was discovered in 2001 [70]. Since then, it has attracted much attention, as a promising material for applications and an interesting one for pure scientific research (for reviews see [71, 72]). $MgB_2$ has a high critical temperature ($39°K$), although it is a conventional phonon mediated superconductor. It also shows strong pinning compared to high temperature superconductors (HTSC) and transparency of grain boundaries to current (absence of weak intergranular links). Finally, it is a simple com-

position of commonly found constituents. This combination of simplicity and abundance of constituents with the expected perfect conductance in intermediate temperature ranges suggests that $MgB_2$ could be developed to a good material for applications.

$MgB_2$ possesses properties of conventional superconductors (e.g. isotope effect) together with properties of high temperature superconductors (e.g. quadratic temperature dependence of the penetration depth) as well as a variety of new properties. Many of the new characteristics are related to its complex two-band Fermi surface (see [73] and articles cited therein). In particular, $MgB_2$ has two distinct superconducting gaps with distinct symmetries. This gives rise to exotic features, for example, a crossover between two regimes in which superconductivity is dominated by either of the bands causes a temperature dependence of the anisotropy parameter $\gamma = H_{c_2}^{ab}/H_{c_2}^{c}$. The value of $\gamma$ varies significantly, depending on the type of measurements (magnetization, transport, heat capacity) and of sample (thin films, polycrystalline, single crystal, powders). This variability suggests a diversity of the mechanisms probed by the different measurements as discussed below, and was one of the motivations for the work presented in section 7.4.

Another unusual property of $MgB_2$ is the pronounced broadening of the resistive transition in an external magnetic field. The origin of this broadening has not been resolved yet. It was suggested to originate from the two superconducting gaps [74], from vortex dissipation and vortex lattice melting [75], from surface barriers [76], superconducting fluctuations [76], or surface superconductivity [77, 78, 79].

### 4.2.4 Physics of the Edges of a Superconductor

#### Surface Superconductivity

As predicted by Saint-James and de Gennes [80] and measured in some classic superconductors [81, 82, 83, 84, 85, 86, 87], there is yet another superconducting phase. In a thin layer close to the surface, superconductivity can still exist above $H_{c_2}$. The width of this thin layer is of the order of the coherence length, $\xi$. A superconducting solution can exist only up to some critical external magnetic field. A higher magnetic field will destroy superconductivity by making the effective potential well steeper, giving the Cooper pairs more kinetic energy, and by that, breaking them into two electrons. The linearized Ginzburg-Landau (G-L) equation for the order parameter, $\psi$, gives rise to solutions with different critical magnetic fields, $H_{c_2}$ and $H_{c_3}$. Solutions which have a critical field $H_{c_2}$ correspond to the ground state in a parabolic potential well and are localized either far from the facet or exactly on it. Solutions

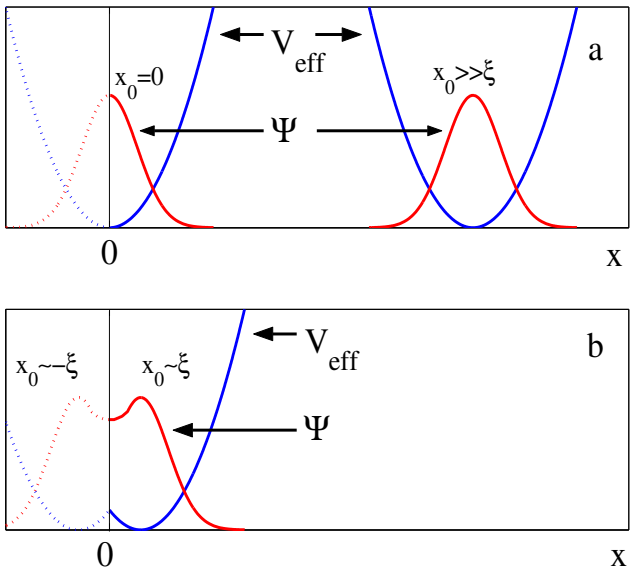


*Fig. 4.7:* **a)** Nucleation of superconductivity in the bulk and on the surface at $H_{c_2}$. **b)** Surface nucleation of superconductivity at $H_{c_3}$

which are localized close to the surface compared to $\xi$, but not exactly on it, correspond to the ground state of a wider and shallower effective potential, and thus have a lower energy. As a result of that, they can exist up to a higher critical field, $H_{c_3}$. It can be understood as follows. For a field parallel to the surface $H \| z$ axis, in a gauge $A_x = A_z = 0$; $A_y = Hx$, the G-L equation can be reduced to an equation which describes a particle in a parabolic potential in $x$, while moving freely in $y$ and $z$ directions. Solutions with different momenta, $\hbar k_y$, correspond to different minimum points, $x_0(k_y)$ of the parabolic potential (see figure 4.7**(a)**). Solutions which are localized either far from the surface compared to $\xi$ or exactly on the surface, automatically satisfy the condition of zero normal current on the surface between a conductor and an insulator

$$\frac{d\psi}{dx} \mid_{surface} = 0 \tag{4.8}$$

However, when $x_0$ is very close to a facet parallel to the field, a Gaussian solution around that point does not satisfy the boundary condition. Nevertheless, another solution exists, which satisfies the boundary conditions. This solution can be found by extending the original potential well outside the surface by a mirror image outside the surface obtaining a symmetric potential well (see figure 4.7**(b)**). The ground state in such a potential well is

also symmetric around the boundary, and thus satisfies both the equation and the boundary condition (equation (4.8)). Since this effective potential is shallower, its ground state is lower than the ground state of a parabolic potential and can exist up to a higher field $H_{c_3}$ before it is destroyed. There does not exist a gauge condition that would give rise to superconducting solutions on a surface perpendicular to the field above $H_{c_2}$. Detailed calculations of the surface nucleation field show that $H_{c_3} \simeq 1.7 H_{c_2}$. In the surface superconducting phase, transport current applied to the sample will flow along the superconducting surface to avoid the resistive bulk.

### *Surface Barriers*

Another important mechanism which can drive current to flow predominantly on the edges is the Bean-Livingston surface barrier (SB) [88]. This barrier is due to the superposition of two forces acting on the vortex in opposite directions and is known to be very sensitive to surface imperfections. The first force is an outward pulling force which may be understood as the action of the fictitious mirror vortex replacing the condition of zero normal current at the boundary between a metal and an insulator. The second force is the repulsion between the penetrating tail of the external field and the vortex. The net result of these two competing effects is a potential barrier near the surface which obstructs vortices on the inside from leaving the sample and those on the outside from entering (figure 4.8).

When current is driven through the sample the Lorentz force it exerts on the vortices causes them to flow in a direction perpendicular both to the current and to the field. In order to maintain a homogeneous motion across the sample, the hopping rate across the surface barrier must be equal to the flow rate in the bulk. If the surface barrier hight is significantly larger than the bulk pinning energy, most of the current will flow at the edges of the sample in order to help drive vortices over the barrier [89, 90, 91, 92], while only a negligible part of it will flow in the bulk and depin vortices there.

### *Edge Contamination*

The presence of substantial surface barriers in $NbSe_2$ [89] is an important ingredient in its edge contamination mechanism [67]. In the presence of transport current, vortices enter a bar-shaped sample through one edge and leave through the other. In the absence of surface barriers, vortex penetration does not require any extra force. As a result, vortices penetrate the sample close to their proper vortex lattice locations, as dictated by the elastic forces of the lattice. However, in the presence of a surface barrier, due

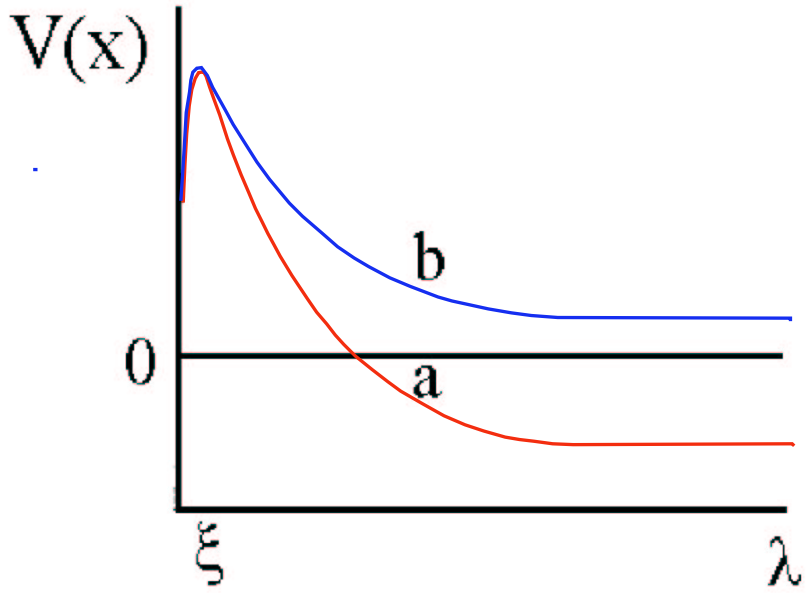


*Fig. 4.8:* The potential energy of a test vortex near the surface for **(a)** flux entry; **(b)** flux exit.

to its inhomogeneous nature, the penetrating vortices are injected at the weakest points of the barrier, thus destroying the local order and forming a metastable disordered vortex phase near the edge. This phase drifts into the bulk of the sample with the flow of the entire lattice which is caused by the Lorentz force exerted by the current in the bulk of the sample. The bulk current serves as effective temperature and anneals the disordered metastable vortex phase. This annealing by an externally applied current was observed in $NbSe_2$ by transport [62, 67], magnetic response [69], decoration [93] and small angle neutron scattering [94] experiments.

The annealing process is sensitive to the location in the $H - T$ phase diagram. In close proximity to the transition, the lifetime of this metastable state, $\tau_r$, is long and annealing occurs over a long healing length, $L_r = v\tau_r$, where $v$ is the vortex lattice drift velocity. At fields farther from the transition, however, the energy difference between the equilibrium quasi-ordered phase and the disordered metastability is larger, thus the lifetime of

the metastable phase, $\tau_r$, becomes shorter. As a consequence, it anneals over a short characteristic $L_r$.

# 5. METHODOLOGY

## *5.1 Shaking*

In BSCCO, non equilibrium irreversible effects mask the underlying thermodynamic behavior throughout a large fraction of the $H-T$ phase space. Experimentally, this is a major obstacle in mapping phase transitions of vortex matter. Moreover, the presence of correlated disorder, even of a low density has been shown to greatly enhance pinning effects throughout most of the solid phase [51, 95]. Consequently, the irreversibility line shifts towards even higher temperatures and fields and further reduces the portion of the phase space which is accessible for equilibrium investigation.

It has been shown that employment of the shaking method in pristine samples of BSCCO suppresses hysteretic effects at fields around the melting transition down to a temperature of 28K, enabling the mapping of the true thermodynamic phase transitions of vortex matter. This method [35, 39, 96, 97] utilizes an in-plane ac shaking field which penetrates the sample in form of in-plane vortices and form a Josephson lattice. These vortices cause weak local agitation to the c-axis pancake vortices, deforming their stacks momentarily and assisting their relaxation process towards equilibrium configuration. Consequently, the portion of the phase space which is accessible for equilibrium investigation is extended.

One could argue that in the presence of columnar defects shaking may also affect the equilibrium properties of vortices. Indeed, in YBCO crystals tilting the magnetic field away from the columnar defects was shown to alter the equilibrium magnetization [98]. In irradiated BSCCO, however, shaking seems to be similarly effective despite enhanced correlated pinning. It was shown that a moderate in-plane field has essentially no effect on its equilibrium properties, even in the presence of columnar defects, due to very high anisotropy [99, 100]. As a result, the ac in-plane field enhances vortex relaxation without altering the thermodynamic transitions [100].

### 5.1.1 Field Alignment

When employing the shaking method, care must be taken in aligning the ac field to reside only within the $a - b$ plane of the sample. This is to prevent smearing of the phase transitions of vortices that may be caused by a stray $c-$axis oscillating field. In our measurements we have examined two alignment techniques: magnetic and mechanical.

1. The Magnetic Technique. Within the magnetic technique an additional synchronized magnetic field of an equal amplitude and an opposing sign was applied in order to cancel the projection of the ac shaking field along the sample's c-axis. It was generated by a coil that was placed on the cup of the sample-space whose current was driven by a separate Kepco amplifier. Synchronized modulation of both the x-axis shaking field and the z-axis cancelling field was done by a two-channel 8904A HP signal generator. The alignment process was monitored with a Hall-sensor residing underneath the sample. Its measurements of the reminiscent projection of the oscillating field on the sample's z-axis was measured with an SR830 lock-in amplifier.

2. The Mechanical Technique. A more straight-forward approach to solving the x-field misalignment difficulty is the mechanical technique. Here, the sample is placed on a stage which can be physically tilted to achieve alignment with the magnet's x-axis. The tilting adjustment is done with the aid of two long screws which are connected to the sample stage within the dewar at one end and extend to the lab level on the other. Here too, the alignment process was monitored with a Hall-sensor residing underneath the sample. Its measurements of the reminiscent projection of the oscillating field on the sample's z-axis was measured with an SR830 lock-in amplifier. This method produced alignment down to $0.8^\circ$ and was found to be simple to employ. We, therefore, chose to utilize it in our measurements.

## 5.2 Hall-Sensor Array

One of the methods to map the phase diagram of vortex matter in type II superconductors is by performing local magnetization measurements. In such measurements, a discontinuity indicates a first-order transition, whereas a break in the slope indicates a second-order transition. For local magnetization measurements we use the local Hall-sensor array technique [101]. This technique employs a two-dimensional electron gas Hall-sensor array, fabricated using photolithographic and etching techniques. These sensors, which

can be manufactured with small dimensions down to $1 \times 1\mu m^2$, have the advantages of a linear response to a magnetic field, weak temperature dependence, and high sensitivity. The sample is mounted onto the surface of the array. A current is driven through the array and the corresponding Hall voltage is proportional to the perpendicular component of the magnetic field within the sensor (see figure 5.1).

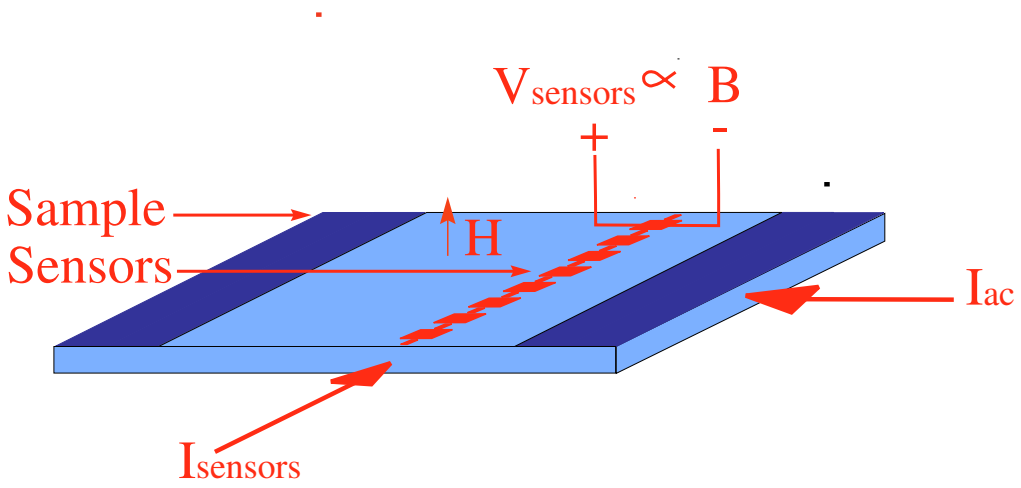


*Fig. 5.1:* Experimental setup with a Hall sensor array. The sensor array is attached to the surface of the sample. dc current, $I_{sensors}$ is driven through the sensors and the measured perpendicular Hall voltage is a linear function of the field inside the sample, $B$. Within the self-field method, an additional alternating current $I_{ac}$ is driven through the sample and the resulting oscillating induced magnetic field, $B_{ac}$, is proportional to $V_{ac}$ measured by the sensors using a lock-in amplifier.

### *5.2.1 Self-Field Measurements*

A measurement approach has been devised in our lab a decade ago [90], which allows determination of the flow pattern of transport current across the sample. As conventional transport measurement cannot reveal where the current flows, the self-field measurement plays a crucial role in the study of the crossover between edge dominated and bulk dominated regimes in the phase diagram of type II superconductors. Within this approach, ac current is driven through the sample. A Hall sensor array at the surface of the crystal picks up the spacial distribution of the ac magnetic field induced by this

current, superimposed on the dc field (see figure 5.1). After filtering out the dc field from the signal by a lock-in amplifier, the current distribution across the sample can be deduced using the Biot-Savart law. We employed this method in our study of surface superconductivity and the phase transition line at $H_{c_3}$ in $MgB_2$.

Presented in figure 5.2 are some typical field distributions $B_{ac}$ (blue lines) that can be obtained in self field measurements and the current distributions $I_{ac}$ (red lines) which generate them:

1. A uniform current distribution within the sample (figure 5.2**d**) produces the field profile in figure 5.2**a**. This profile is expected to occur in the normal phase.

2. When current flows predominantly on the edges of the sample (figure 5.2**e**) the self field profile within the sample is sign-inverted (figure 5.2**b**) compared to the profile of the evenly distributed flow. This profile is expected when the temperature is in the range $T_{c_2}(H) < T < T_{c_3}(H)$ and only the surface of the sample is in its superconducting phase. In addition, it may be expected in regions where surface barriers dominate the current flow.

3. In the regions of strong pinning and in the Meissner phase (figure 5.2**f**), the self induced field, $B_{ac}$ is expelled from the sample (figure 5.2**c**).

## 5.3 Columnar Defects

In order to study the effect of correlated disorder on the vortex matter phase diagram we introduced columnar defects to samples of the high temperature superconductor BSCCO and the low temperature superconductor $NbSe_2$. This is done by irradiating the samples with heavy ions which leave damage tracks behind them. Both BSCCO and $NbSe_2$ samples were bombarded with Pb ions with an energy of 1GeV at several densities between a matching field of $B_\phi = 5$G and $B_\phi = 500$G. All samples were partially masked during irradiation. It allowed a direct comparison between pristine and irradiated behavior. Irradiation sessions took place at the national heavy-ion accelerator in France (GANIL).

## 5.4 Transport Measurements

The natural way to investigate the behavior of the critical current is to conduct V-I measurements. We thus performed four probe transport measurements in our investigation of the peak effect in the critical current of $NbSe_2$.

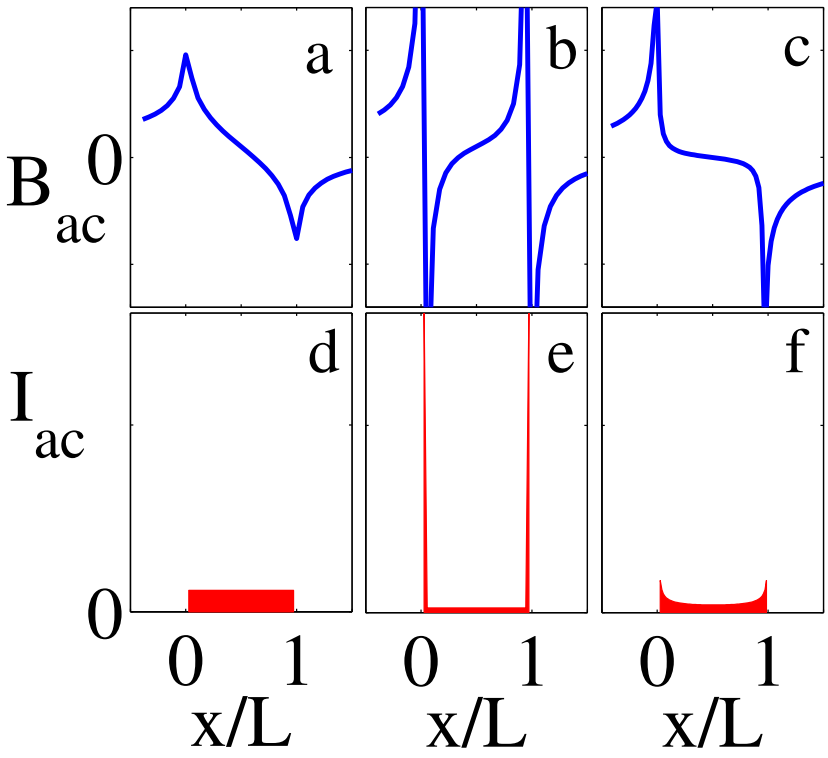


*Fig. 5.2:* Typical current distributions in the sample (bottom) and the corresponding expected field profiles $B_{ac}(x)$ (top) calculated using the Biot-Savart law. A uniform flow across the sample (**d**), e.g. in the normal phase, produces the self-field profile in (**a**). When practically all the current flows at the edges of the superconductor (**e**), the field inside the sample has an inverted profile relative to the field profile of a uniform-current-flow (**b**), e.g. in the surface barrier dominated regime and the surface superconducting phase. When strong bulk pinning is present and in the Meissner phase (**f**), a vanishing $B_{ac}$ signal is expected within the sample (**c**).

Current through the two external contacts is increased from zero at a constant temperature and external field. The resulting voltage is measured between the two internal contacts on the pristine side and these on the irradiated side,

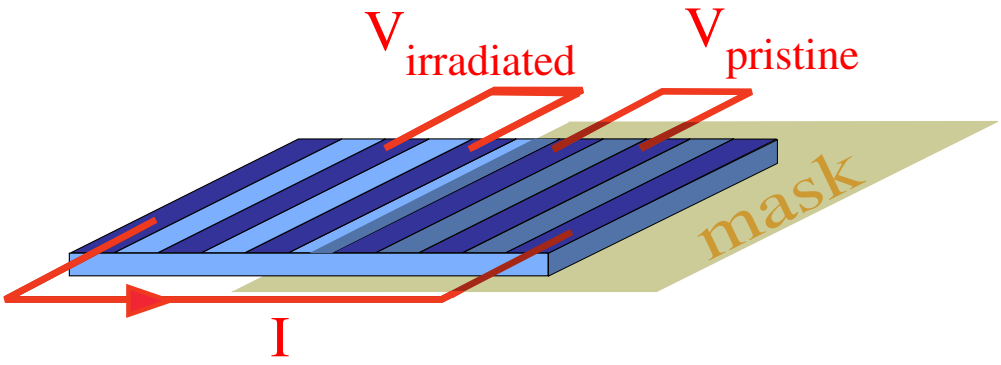


*Fig. 5.3:* The half irradiated sample geometry. Six gold contacts were evaporated on each $NbSe_2$ sample in order to allow transport measurements on both pristine and irradiated areas.

simultaneously at each current step.

We found that currents of magnitude relevant to our study cause unwanted heating of the sample due to relatively high contact resistance of several Ohms. This change in temperature, which can be as large as several tenths of a degree, can make data interpretation ambiguous. In order to minimize the problem of heating we stabilized temperature in presence of transport current. We did this with the help of a temperature sensor installed in very close proximity to the sample. In this scheme we use the cooling power of the system to compensate for the unwanted heating by the current.

## 5.5 Sample Preparation

Three of the BSCCO samples used for the study of its $H-T$ phase diagram in the presence of columnar defects (section 7.1) were optimally doped with $T_c \approx 92$K [102]. Before irradiation with a matching field of $B_\phi = 5, 10$ and 20G they were cleaved and cut into rectangles of dimensions $1100 \times 500\mu m^2$, $1300\times450\mu m^2$ and $950\times450\mu m^2$ respectively. During the irradiation about two thirds of each sample was covered by a stainless steel mask of $50\mu$m thickness, in order to allow a direct comparison between pristine and irradiated behavior. An additional, slightly under-doped sample ($T_c \approx 91$K)

with a matching field of $B_\phi = 20$G was cut to a rectangle of dimensions $650 \times 2250\mu\text{m}^2$. This sample was irradiated through a mask with circular holes of $80\mu$m diameter. All samples had thickness of about $50\mu$m.

In Section 7.2 the slightly over-doped sample ($T_c \approx 90$K) was grown using the travelling solvent floating zone method [103] and polished into a triangular prism shape of base $270 \times 660\mu\text{m}^2$ and height $70\mu$m. Additional BSCCO samples [102] with different stoichiometries were measured. A slightly under-doped crystal ($T_c \approx 88$K) was cut into a rectangle with dimensions of $220 \times 740\mu\text{m}^2$. An optimally doped ($T_c \approx 92$K) crystal and an over-doped ($T_c \approx 88$K) crystal were cut into disks with diameters $400\mu$m and $600\mu$m respectively. A higher over-doped crystal ($T_c \approx 85$K) was cut into a square with $230\mu$m and $400\mu$m sides respectively. All samples had thickness of about $50\mu$m.

The $NbSe_2$ samples which were used in section 7.3 had typical dimensions of $1700\times600\times15\mu\text{m}^3$ and critical temperature $T_c \approx 7$K. They were irradiated with matching fields in the range $B_\phi = 5 - 60$G. During irradiation half of each sample was covered by a stainless steel mask of $50\mu$m thickness.

The results presented in section 7.4 were obtained using two single crystals of $MgB_2$ [104, 105, 106], A and B. The dimensions of sample A were $100 \times 80\times50\mu\text{m}^3$ whereas those of sample B were $270\times135\times50\mu\text{m}^3$. Their critical temperature was $T_c \approx 37$K.

Mounting the samples on Hall sensors (see figure 5.4a) for magnetization and self-field measurements was done using Alessi Rel-4100A probe station, which enabled placing the crystals within $1\mu$m resolution. A small amount of wax (Nanodecane) with melting temperature $30 - 90°$C was used to glue the crystals to the sensors. This was particularly convenient for moving samples and replacing sensors, as the wax was easily melted by heating with a simple coil heater. The GaAs sensor chip was attached to the chip carrier using Varnish for good thermal conductivity.

In section 7.3, six electric contacts were applied to each $NbSe_2$ sample using the flip-chip method (see figure 5.4c), in order to allow transport measurements. Within this method, the relatively small gold pads of the crystals are extended by longer pads on a transparent sapphire substrate to which they are glued by silver epoxy for electric conductivity. These pads, in turn, were electrically connected to those of the chip carrier in a simple manner using a bonding station. The gold pads were evaporated on the crystals and the substrates through specially designed brass masks. The crystals were held steady by the probe station while the substrates were carefully placed on top, pads down. The transparency of the sapphires enables an accurate alignment of the gold pads of the crystals and those of the substrates. This method rendered typical contact resistances of $2 - 10\Omega$ at room temperature.

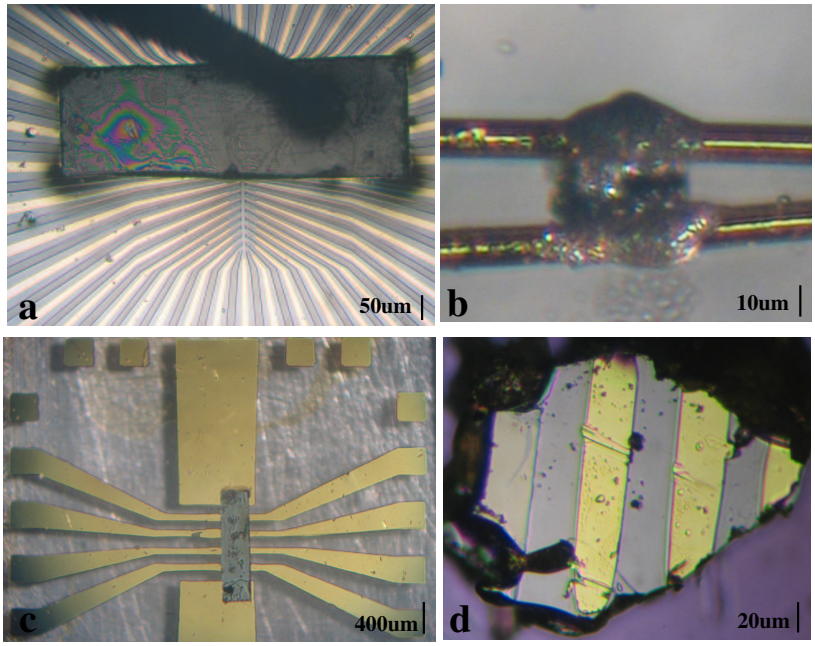


*Fig. 5.4:* (a) A BSCCO sample mounted on a Hall sensor chip. (b) $MgB_2$ crystal A with thin gold wires of 12$\mu$m diameter glued to its two gold pads with silver epoxy. (c) The gold pads on the bottom surface of a $NbSe_2$ crystal glued to the gold pads on a sapphire substrate by the flip-chip method. (d) $MgB_2$ crystal B with four gold pads.

In section 7.4, $MgB_2$ single crystals [104, 105, 106] each with two to four electric contacts (see figure 5.4b and d) were used in order to allow self-field measurements. As crystals were to be mounted on GaAs sensor chips, the flip-chip method could not be used in order to extend contacts to the chip carrier level. Instead, thin gold wires of 12$\mu$m diameter were attached to the samples' gold pads using silver epoxy (see figure 5.4b). The samples were glued to the Hall sensor chip with UV NOA glue. The gold wires were then bonded to the pads of the chip carrier using a bonding station. This method rendered typical contact resistances of 10$\Omega$ at room temperature.

# 6. EXPERIMENTAL SETUP - CRYOGENICS AND MAGNETICS

The cryogenic system (see figure 6.1) is composed of a Helium flow cryostat placed inside a dewar filled with liquid Helium. It is planned to allow stabilization of the temperature of the sample in the range between 4.2K and 150K. Helium flows from the dewar into the cryostat due to a pressure difference between the two. The pressure of the dewar is maintained at a typical value of 5 psi with a pressure valve. The flow of Helium is regulated by a needle-valve at the entrance of the cryostat and a flow-meter at its exit. This flow of Helium into the sample space is responsible for its cooling. Heating to the desired temperature is done by two coil heaters. One heater is located

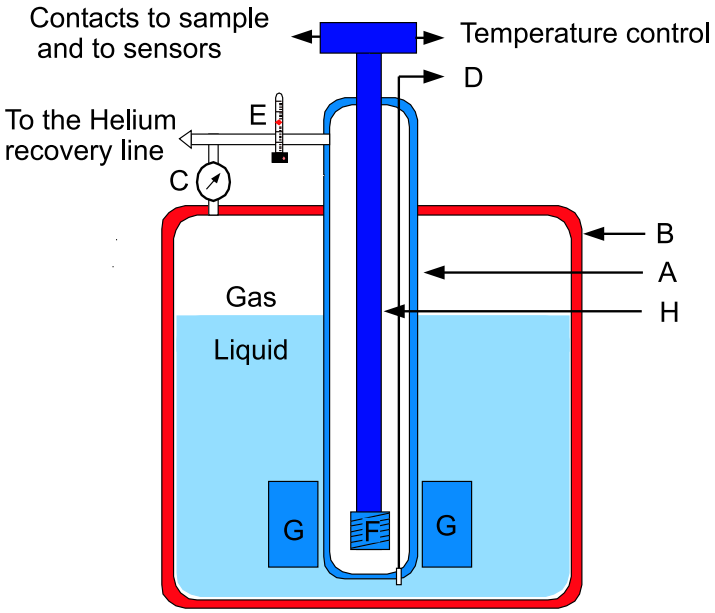


*Fig. 6.1:* The cryogenic and magnetic systems. (A) cryostat (B) dewar (C) pressure valve (D) needle valve, heater and temperature sensor (E) flow meter (F) sample space and heater (G) magnets (H) rod.

within the cryostat near the opening through which the Helium enters the sample space, whereas the other is located in close proximity to the sample. The temperature is measured with two diode sensors which are located one near each of the heaters and is monitored and stabilized with two Lakeshore temperature controllers. The walls of the cryostat are vacuum-pumped in order to achieve thermal isolation.

The external magnetic fields were applied along two perpendicular axes (the x-axis and the z-axis) of the sample using two separate superconducting magnets which are placed inside the dewar and surround the bottom part of the cryostat. During measurements in which the shaking method was utilized, the in-plane ac shaking field was generated by the x-axis coil. The current to it was driven by a Kepco amplifier, which was modulated by HP 8904A signal generator. The shaking field was typically at a frequency of 10Hz and had a maximal amplitude of 350G.

The sample and Hall sensors are mounted on one end of a sample rod which is inserted into the the sample space within the cryostat. Electric contacts to the Hall sensors, to the sample itself and to the temperature sensor which is placed near it are connected through coated wires to the connectors at the top of the rod.

# 7. RESULTS AND DISCUSSION

## *7.1 Multiple Changes of Order of the Vortex Melting Transition in $Bi_2Sr_2CaCu_2O_8$ with Dilute Columnar Defects*

In this section we study the evolution of the first-order melting transition of vortices in BSCCO with the introduction of correlated disorder. Our findings reveal that a SO transition is nucleated in a small segment along the FO transition line, bound by two critical points. This SO segment grows with increasing the density of the columnar defects providing an important insight into the general mechanism of transformation of a FO transition into a SO transition.

We mapped for the first time the *equilibrium* phase diagram of vortex matter with dilute columnar defects by performing local magnetization measurements during vortex shaking. We measured three BSCCO samples with matching fields of $B_\phi = 5\text{G}, 10\text{G}, 20\text{G}$ and critical temperature $T_c \approx 92\text{K}$ and an additional sample with $B_\phi = 20\text{G}$ and $T_c \approx 91\text{K}$. Two thirds of each sample was masked during irradiation to allow a direct comparison between pristine and irradiated behavior. The local magnetic induction of the sample was measured by an array of Hall sensors 10x10 $\mu\text{m}^2$ each, while sweeping the external magnetic field $H$ at a constant temperature. Simultaneous measurements of the transition on the pristine halves of the samples show that it remained FO throughout the temperature range. Shaking fields up to 350G at 10Hz were used.

Figure 7.1 presents the measured local magnetization, $B-H$, at (a) 90K, (b) 84K and (c) 42K. A FO transition appears as a sharp step in $B(H)$ and a SO transition is manifested by a break in its slope. To better resolve the nature and location of the phase transition we differentiated the measured induction $B$ with respect to the applied field $H$. Figure 7.2 shows the derivatives $dB/dH$ of representative (a) high temperature, (b) intermediate temperature and (c) low temperature measurements. A $\delta$-like peak in the derivative $dB/dH$ indicates a FO transition, whereas a discontinuity signifies a SO transition.

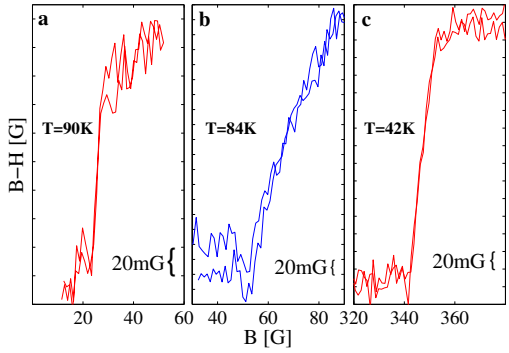


*Fig. 7.1:* The measured local magnetization, $B-H$, of the $B_\phi = 10$G sample in the presence of shaking, measured upon ascending and descending external field at constant temperatures of (a) 90K, (b) 84K and (c) 42K. A linear slope was subtracted for clarity. A sharp step in the local magnetization in (a) and (c) signifies a FO transition. In (b), a break in the slope signifies a SO transition.

At high temperatures we find that the transition remains FO in the presence of columnar defects, similarly to that in the pristine areas, as previously reported [49, 51]. Accordingly, $B(H)$ in Fig. 7.1a shows a sharp step and the derivatives $dB/dH$ in Fig. 7.2a display a $\delta$-like peak. At a slightly lower temperature thermal fluctuations are weaker, the effective pinning potential of the columnar defects gains strength and irreversibility is greatly enhanced, thus masking the underlying phase transition. We overcame this problem by applying the shaking method rendering a reversible magnetization [35, 39, 96, 97]. Figures 7.1b and 7.2b thus show equilibrium measurements at intermediate temperature of $B - H$ and $dB/dH$, respectively. A break in the slope of the induction is clearly resolved along both ascending and descending field sweeps and the derivatives display a step structure indicating a SO transition.

Yet, our main finding is the recovery of the FO thermodynamic phase transition at lower temperatures. This is clearly visible in Fig. 7.1c as a reversible discontinuity in magnetization $B(H)$ and accordingly, in Fig. 7.2c a sharp peak in the derivatives $dB/dH$. This recurrence of the FO nature of the transition has been predicted theoretically [46], but was never observed experimentally.

These findings can be explained by the following comparison of energy scales. At high temperatures thermal fluctuations are dominant enough to weaken the effective pinning potential due to columnar defects [45, 46, 47, 48, 49, 51, 52, 100, 107, 108, 109], resulting in a FO transition similar to that found in pristine samples. At intermediate temperatures, as correlated pin-

ning gains dominance, the randomly distributed columnar defects alter the *equilibrium* vortex matter state, in addition to enhancing irreversible hysteretic behavior. At these temperatures the melting occurs at intermediate fields $B_m > B_\phi$ and the pristine Bragg glass phase is replaced by a porous solid with crystallites of interstitial vortices imbedded in the pores of a rigid amorphous vortex matrix [49, 52, 100]. The size of the nanocrystals within

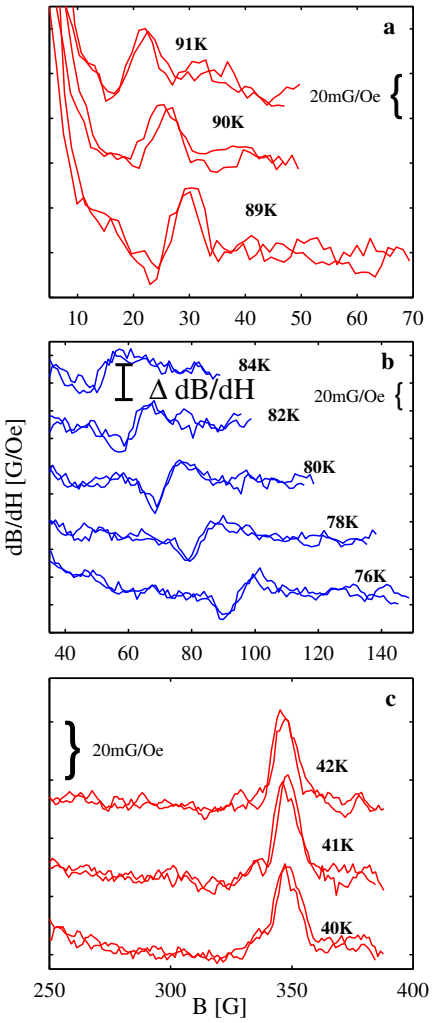


*Fig. 7.2:* The derivative of the measured induction with respect to applied field, $dB/dH$, of the $B_\phi = 10$G sample in presence of shaking, measured upon ascending and descending field at constant temperatures of (a) 89K – 91K, (b) 76K – 84K and (c) 40K – 42K. Data are shifted vertically for clarity. A peak in $dB/dH$ in (a) and (c) signifies a FO transition, whereas a step in (b) indicates a SO transition.

each pore is only several times their lattice constant. These dilute nanocrystals seem to melt into nanodroplets through a SO transition probably since the range of correlations is cutoff by the finite size of the pores, consistent with recent numerical simulations [47, 48, 107, 108]. This is similar to the dense columnar defect limit, where correlated pinning dominates and vortex matter undergoes a second order BoG transition.

At low temperatures $\sim$ 40K the transition occurs at high fields. Each

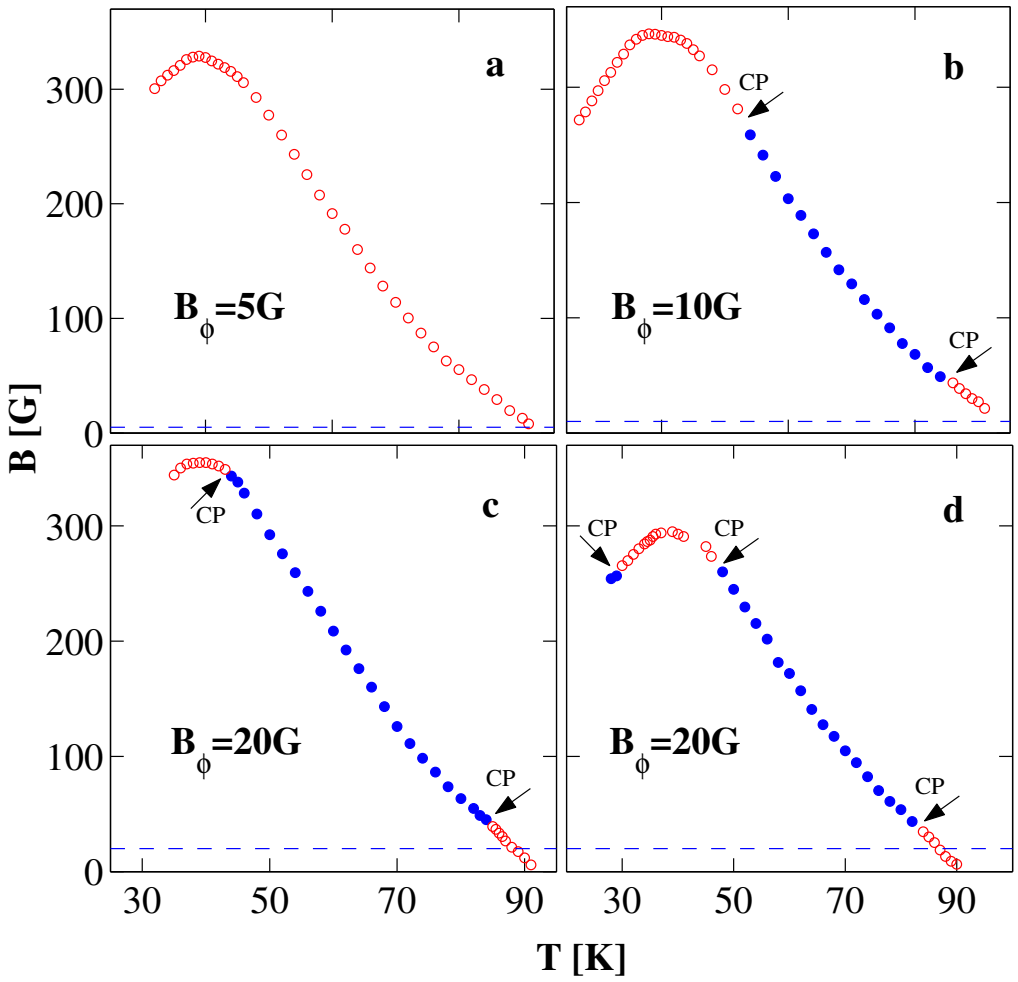


*Fig. 7.3:* Phase diagrams of irradiated BSCCO crystals showing FO (○) and SO (●) transitions. (a) In $B_\phi$ =5G sample the transition is FO at all temperatures. (b) For $B_\phi$ =10G a FO-SO-FO behavior is found. (c) The SO segment expands in $B_\phi$ =20G sample. (d) A different $B_\phi$ =20G sample with lower doping that exhibits a FO-SO-FO-SO sequence. The values of $B_\phi$ are shown by dashed lines.

pinned vortex is surrounded by tens of interstitial vortices and the solid phase is increasingly dominated by inter vortex interactions [46], resulting in relatively ordered dense vortex crystallites [52]. Consequently, their melting into nanodroplets is accompanied by a discontinuity in the entropy that reflects the sharp difference in ordering of the two phases. The FO nature of the transition is thus restored, as in pristine samples.

Note that at intermediate temperatures, where the transition is SO, the step in the derivative is positive, $\Delta\partial B/\partial H > 0$ (see Fig. 7.2b). This is consistent with a positive step in the specific heat, $\Delta C_v > 0$ which was found in the high-field SO transition of pristine YBCO [110, 111]. It is in contrast, however, to the negative step of the derivative, $\Delta\partial B/\partial T < 0$, at the SO glass transition reported in pristine BSCCO [39]. Further study is required in order to explain the origin of these differing signs.

Interestingly, at intermediate temperatures $dB/dH$ takes a more intricate shape; rather than a simple upward jump, it first decreases, then jumps up and finally slightly decreases again. This structure may be explained by the association of the step in the derivative at the SO transition with the relative ordering of the two phases across the transition line. Then, the decrease in the derivative might be interpreted as a slight ordering of interstitial vortices prior to the major disordering upon melting. A similar feature has been observed in the structure factors in Monte-Carlo simulations [47]. It is yet unclear, however, how these possible structural changes should affect the equilibrium magnetization.

The location and nature of the transition of the four samples was measured and mapped. Shaking enabled the detection of a melting transition down to 27K. The results are summarized in Fig. 7.3. The FO and SO regions are marked by open and solid circles respectively. In all four irradiated samples, the location of the melting line remained similar to that of the pristine parts of the samples, with a maximum at $\sim$ 40K. The 5G sample exhibits a FO transition at all temperatures. As the density of columnar defects is increased, more of the $B-T$ phase space becomes dominated by correlated disorder and consequently, a larger portion of the transition line becomes SO. The 10G and 20G samples both display two CPs with a FO-SO-FO sequence. In the 20G sample the two CPs are shifted further apart than in the 10G sample and the SO transition spreads both to high and low temperatures. We therefore suggest that this trend persists until a full SO BoG transition line is attained in the dense-pin limit.

Note that the FO transition line of irradiated samples persists to the left of its maximum in the inverse melting region (Fig. 7.3). These are the first equilibrium magnetization measurements in this region in presence of columnar defects. Figure 7.3d shows the phase diagram of a sample with $B_\phi = 20$G

and a slightly lower oxygen doping. This sample displays even more intricate behavior. Like the other $B_\phi = 20$G and 10G samples, it also exhibits FO-SO-FO behavior. In addition, this sample reveals a third CP at extremely low temperatures on the inverse melting side of the transition. Below this CP we observe a recurrence of the SO nature of the transition. It can be attributed to the fact that the melting field decreases in the inverse melting region with decreasing T. As a result, nanocrystals contain less vortices and correlated pinning regains dominance over elasticity. Consequently, the transition becomes SO once again, similarly to that at intermediate temperatures.

It is worth pointing out the qualitative difference between the behavior reported here and the SO-FO-SO sequence found in pristine samples of the less anisotropic YBCO compound [110]. In irradiated BSCCO all three portions of the transition line separate a solid phase from a liquid phase. In pristine YBCO, however, the high-field SO portion is believed to separate two liquid phases due to the existence of a tri-critical point [111]. The low field SO portion, on the other hand, separates a solid phase from a liquid phase and is believed to arise from the intrinsic correlated disorder in YBCO crystals [112, 113].

## 7.2 Interplay of Anisotropy and Disorder in the Doping-Dependent Melting and Glass Transitions of Vortices in $Bi_2Sr_2CaCu_2O_8$

Here we study the oxygen doping dependence of the first order melting and second order glass transition lines of vortices in BSCCO. We show that the SO line scales with material anisotropy even where the FO line does not, and that effective disorder weakens with doping, but gains relative dominance over thermal fluctuations.

We present measurements of slightly under-doped (SUD), optimally doped (OPD), slightly over doped (SOD), over doped (OVD) and highly over doped (HOD) BSCCO crystals [102, 103] with critical temperatures $T_c$ =88, 92, 90, 88.5 and 86 K, respectively. Various crystal geometries were studied with typical sizes of $\sim 300\times300\times40$ $\mu$m$^3$. They were mounted on $10\times10$ $\mu$m$^2$ Hall sensor arrays, fabricated in a GaAs/AlGaAs heterostructure. At low temperatures we utilized a 350 Oe in-plane *ac* shaking field of 10 Hz to relax the pancake vortices towards their equilibrium configuration [35, 39, 96]. Conjugating local probes with shaking yielded the equilibrium reversible magnetization of the samples.

Figure 7.4 shows the local induction $B(H)$ measured in the SUD sample by sweeping the external magnetic field, $H$ at various constant temperatures.

The external field, $H$, was subtracted to flatten the originally increasing local induction. In these sweeps the FO melting transition is manifested by a discontinuous step in the magnetization. Figure 7.5 shows the local induction $B(T)$ measured in this sample by sweeping the temperature, $T$, at a constant out-of-plane field, $H = 305$Oe, in the presence of an in-plane shaking field. A linear term, $aT$, was subtracted from the measured local induction. A SO phase transition is indicated by an arrow and is manifested by a break in the slope of the magnetization.

We mapped the location of the FO and SO singular behavior of the four samples in the B-T plane. The result is plotted in Fig. 7.6. The melting line shifts as a whole to higher fields with doping due to the decrease in anisotropy, which implies stronger inter-layer coupling and higher stiffness of the pancake vortex stacks [53, 54, 102, 114]. As the FO line shifts to higher fields, its maximum shifts towards increasingly higher temperatures (Fig. 7.6 inset). Identifying these maxima with the crossover from disorder to thermally dominated behavior [29, 30, 36, 115, 116] may suggest that doping enhances disorder. The SO transition line also shifts upwards, further signifying that disorder is enhanced with doping. However, we will show below that this conclusion is inaccurate. Moreover, arguing naively that the balance between characteristic energies constrains the SO line to bisect the

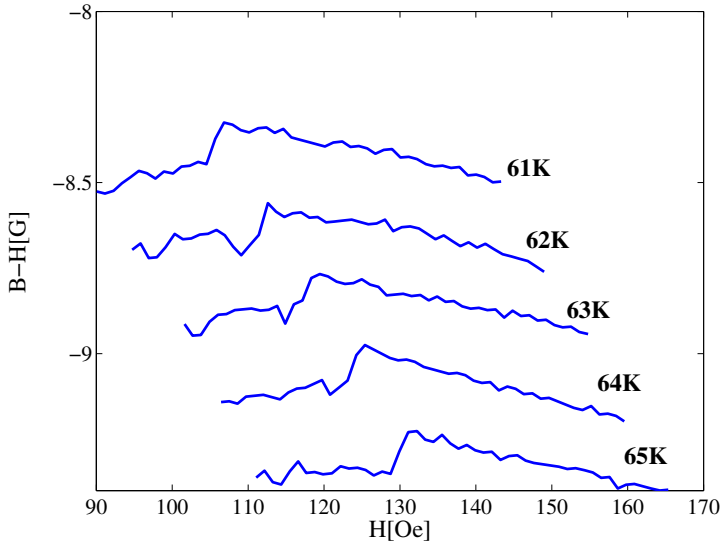


*Fig. 7.4:* The local induction $B(H)$ measured in the SUD sample by sweeping the external magnetic field, $H$ at various constant temperatures. The external field, $H$, was subtracted. The step in $B(H)$ indicates a first-order transition.

FO one at its maximum [30] is also too simplistic. The inset of Fig. 7.6 clearly shows that in over-doped samples the bisection point resides below the FO maximum temperature (the overlap of the two in the OPD sample is apparently accidental). Therefore, a naive description of thermal depinning cannot account for both the SO line and the FO maximum behavior (for instance, the latter is directly affected also by elasticity) [36, 115, 116].

We now present a quantitative scaling analysis of the doping dependence, parameterized by the sample anisotropy ratio $\varepsilon^2 = m_{\rm ab}/m_{\rm c}$ ($m_i$ is the electronic effective mass in the $i$th direction). For high-$\kappa$ superconductors, such as BSCCO, the Ginzburg-Lanadau (GL) free energy functional can be recast into an isotropic ($\varepsilon = 1$) form by rescaling its parameters [4]. We focus on one such transformation [117] that rescales space, magnetic induction, the penetration depth $\lambda_0$ and the coherence length $\xi_0$. Models for high-temperature melting are usually independent of $\xi_0$, and find $\lambda_0$ to enter with some model-dependent power as a proportionality factor. For definiteness we resort to

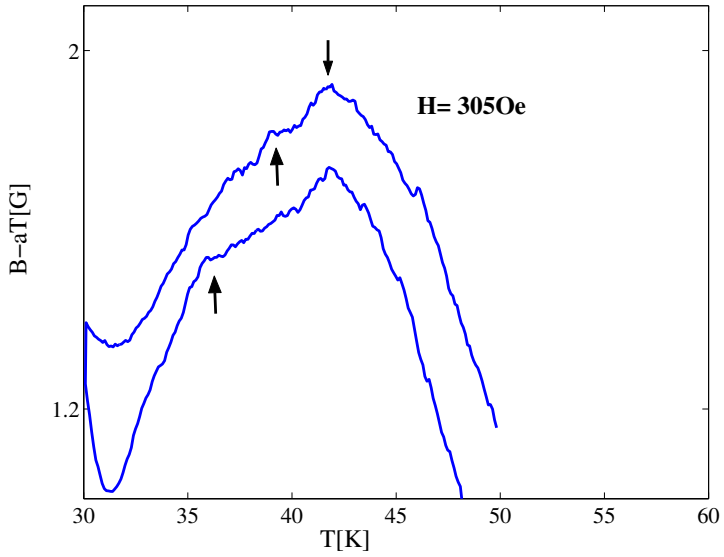


*Fig. 7.5:* The local induction $B(T)$ measured in the SUD sample by sweeping the temperature up and down, $T$, at a constant out-of-plane field, $H = 305$Oe, in the presence of an in-plane shaking field. A linear term, $aT$, was subtracted from the measured local induction. The second-order phase transition is indicated by a downward-pointing arrow and is manifested by a break in the slope of the magnetization $B(H)$. The first-order transitions of the melting and inverse melting regions are appear as an upward and a downward step in $B(H)$, respectively, and are indicated by upward-pointing arrows.

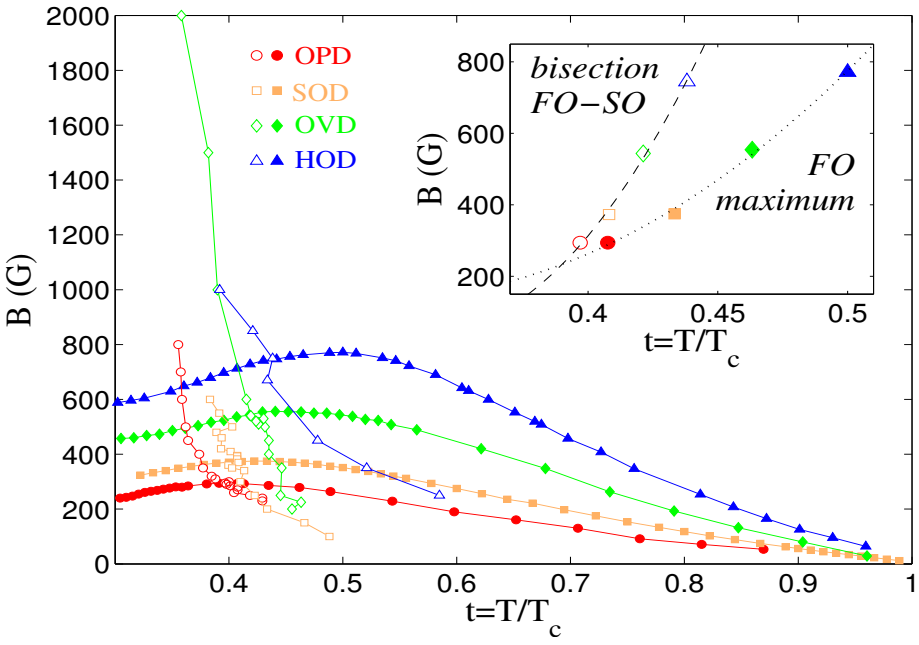


*Fig. 7.6:* FO and SO transition lines (solid and open symbols, respectively) measured with OPD (∘), SOD (⊓), OVD (◇) and HOD (△) samples. The inset shows the doping dependence of the maximum of the FO line and its bisection with the SO line. Dotted and dashed lines are second-degree polynomial fits.

a specific model [118, 119] for a FO evaporation line with no disorder from vortex solid to pancake gas $B_{\rm E}(t) \propto (\varepsilon^2/\lambda_0^2 d)(1-t^2)/t$, where $t = T/T_c$ and $d$ is the inter-plane separation. The scaling transformation [117] indeed renders $B_{\rm E}(t)$ isotropic.

Figure 7.7 shows the rescaled FO and SO lines. The high-temperature parts of the FO lines are perfectly collapsed by dividing their induction axes by a constant [54]. $B_{\rm E}(t)$ (dashed-dotted line) fits the collapsed melting lines precisely, asserting that the multiplicands in this procedure are $(\varepsilon_\circ/\varepsilon)^2$, normalized by the OPD $\varepsilon_\circ^{-1} \approx 500$ [120]. Anisotropy scaling collapses the data down to $t_{\rm th} \approx 0.58$. Below $t_{\rm th}$, which appears to be independent of anisotropy, the rescaled FO lines disperse again, and the fit to $B_{\rm E}(t)$ breaks. The flattening of the FO line towards an inverse-melting behavior results from quenched disorder, which gains dominance with decreasing temperatures [30]. Accordingly, above $t_{\rm th}$ the FO transition is purely thermally-induced, and completely unaffected by disorder [41]. Just below $t_{\rm th}$ disorder becomes a relevant, though not yet a dominant, energy scale.

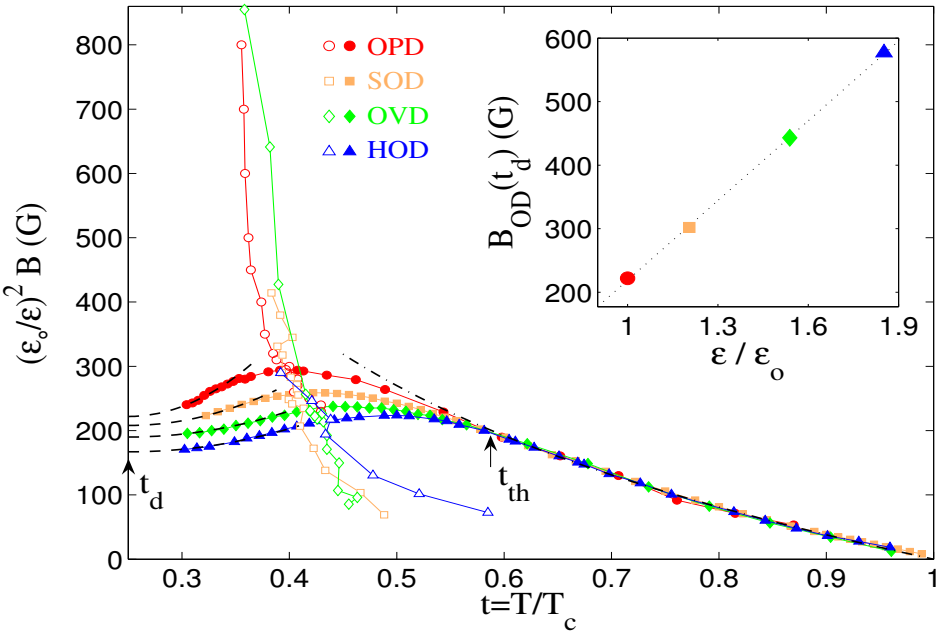


*Fig. 7.7:* Data collapse of the over-doped high-temperature ($t > t_{\rm th}$) FO lines (solid symbols) onto the OPD line, which also collapses the SO lines (open symbols). The fit to $B_{\rm E}(t)$ (dashed-dotted) sets the anisotropy ratios $\varepsilon/\varepsilon_\circ$ to 1, 1.20, 1.54 and 1.85 for the OPD (○), SOD (□), OVD (◇) and HOD (△) samples, respectively. The inset shows the linear dependence of the characteristic $B_{\rm OD}(t_{\rm d})$ on $\varepsilon/\varepsilon_\circ$ (dotted line).

This counterparts the extremely low-temperature behavior, where thermal energy becomes negligible relative to pinning, resulting in a flat temperature-independent behavior of the FO lines [30]. Indeed the FO lines in Fig. 7.7 tend to flatten towards their ends, below which 350 Oe - 10 Hz shaking is insufficient for detecting a reversible melting step. We thus conjectured a similar doping-independent threshold temperature $t_{\rm d} \approx 0.25$, below which thermal energy becomes irrelevant. We fitted the low-temperature order-disorder lines by a leading order expansion $B_{\rm OD}(t \sim t_{\rm d}) \sim B_{\rm OD}(t_{\rm d}) + \Lambda(t - t_{\rm d})^2$, which agrees very well with measurement. We can, therefore, estimate $B_{\rm OD}(t_{\rm d})$, at which elasticity is balanced solely by the disordering potential. It increases monotonically with doping (inset of Fig. 7.7), stating that with reducing anisotropy elasticity gains dominance also over disorder.

Yet, the most remarkable outcome of the anisotropy scaling shown in Fig. 7.7 is the simultaneous collapse of the SO transition lines (with zero freedom). The SO lines reside in a temperature region where anisotropy

scaling of the melting lines fails due to effects of disorder. Still, the same scaling transformation somehow succeeds in rendering the glass-transition isotropic, even though this transition is believed to be intimately related with the competition between disorder and thermal fluctuations.

To gain deeper understanding of the low-temperature behavior we fit the measured transition lines to those predicted by a recent calculation [40], which gives access to the doping dependence of the model's free parameters. It incorporates thermal, disordering and elastic energies to yield bisecting FO and SO lines. The pancake vortex system is modeled by the 2D GL theory. We interpret this single layer model as the outcome of an integration of all other layers out of a complete 3D theory, resulting in an effective 2D model whose renormalized coefficients may still depend on anisotropy $\varepsilon$ of a 3D mass tensor.

The free energy functional is averaged over gaussian disorder in the coefficients of the quadratic and quartic terms using the replica method. Taking the lowest-Landau-level (LLL) approximation yields for the replicated partition function

$$\overline{\mathcal{Z}^n} = \int_{\Psi_1 \ldots \Psi_n} \exp\Big( - \sum_a G_0(\Psi_a) + \sum_{a,b} \tilde{R} |\Psi_a|^2 |\Psi_b|^2 \Big),$$

$$G_0(\Psi) = \int \frac{d^2x}{4\pi} \left( a_T |\Psi|^2 + \frac{|\Psi|^4}{2} + \frac{\kappa^2 (b-h)^2}{\pi \sqrt{2Gi} bt} \right),$$

where $\tilde{R} = a_T^2 b R / 32\pi^2$, $R$ is the disorder amplitude in the coefficient of the quadratic LLL term, $b = B/\tilde{H}_{c2}$, $a_T = (b + t - 1)/(2\pi^2 b^2 t^2 Gi)^{1/4}$ is the LLL parameter, $Gi$ is the effective Ginzburg number that generally scales thermal fluctuations, and $\kappa$ is the GL parameter. Randomness in the coefficient of the quartic LLL term, although crucial for obtaining the non-analyticity of SO, has negligible effect on the locus of the transition lines, and is therefore neglected in the present context.

The FO line is calculated by equating the energies of the homogeneous and crystalline states under the influence of disorder in gaussian approximation. This extends beyond the earlier calculation, which treated disorder perturbatively [34]. The glass line is found from the stability analysis of the replica symmetric solution. The replica symmetry breaking (RSB) is continuous. The corresponding Parisi function describing the hierarchial structure of the glassy state and its detailed derivation can be found in Ref. [40].

The model's free parameters are $R$, $Gi$, $\tilde{T}_c$, and $\tilde{H}_{c2} = T_c \frac{dH_{c2}}{dT}|_{T_c}$. However, due to a hidden symmetry, given by $Gi/\tilde{H}_{c2}^2$ and $Gi/R^2$, the theory effectively has only three independent fitting parameters. We therefore fixed $\tilde{H}_{c2}$ =100T, for simplicity, consistent with our limited range of hole con-

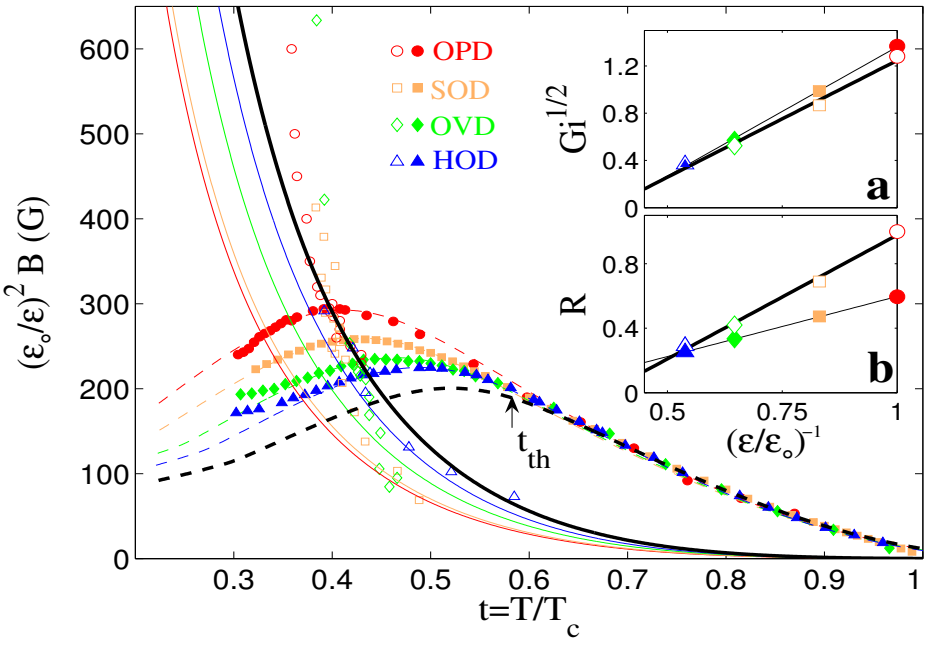


*Fig. 7.8:* Fits of FO (dashed) and SO (solid) lines of the LLL 2D GL model with $\tilde{H}_{c2}$ =100 T, $\tilde{T}_c$ =103, 101, 98 and 95 K for the OPD (○), SOD (□), OVD (◇) and HOD (△) samples, respectively. The values of $Gi$ (**a**) and $R$ (**b**) were fixed either by fitting the SO lines and FO ones above $t_{\rm th}$ (thick lines) or by fitting the full FO lines (thin lines).

centrations [121]. Figure 7.8 presents two fitting strategies motivated by different physical behaviors. The first (thick lines) is optimized to fit the collapsed parts of the phase diagram - SO lines and FO ones for $t > t_{\rm th}$. Interestingly, this set simultaneously provides a collapsed FO line also for $t < t_{\rm th}$. This results from the above symmetry of the model in which $Gi$ and $\varepsilon$ take the same role, defining a relation $R \propto \sqrt{Gi}$ along which the calculated phase diagram remains unchanged under anisotropy rescaling. The thick lines in Fig.7.8 insets show the resulting parameters $Gi = 3.91(\varepsilon_0/\varepsilon - 0.37)^2$ and $R = 1.54(\varepsilon_0/\varepsilon - 0.37)$. The departure of the calculated FO line (thick dashed) from the measured ones below $t_{\rm th}$ may indicate that theory lacks a symmetry-breaking mechanism once anisotropy scaling breaks in experiment.

An alternative fit (thin lines), faithful to the complete FO lines, dictates the slightly different set of values $Gi = 4.77(\varepsilon_\circ/\varepsilon - 0.38)^2$, $R = 0.75(\varepsilon_\circ/\varepsilon - 0.2)$ (insets, thin lines). The excellent fit of the FO lines (dashed) suggests that the effective 2D model still captures the essential physics involved. Its validity should break down at very low temperatures, where indeed it misses

the flattening of the FO lines as $t_d$ is approached, and close to $T_c$ due to critical fluctuations, which may explain the 10% overestimate in the fitted bare $\tilde{T}_c$ values [122]. Substituting this set of values in the calculation of the RSB lines (solid) with zero freedom also produces a good fit that improves with doping, but misses the anisotropy rescaling of the measured SO lines. Nevertheless, the discrepancy between the two sets of values of the different fitting strategies is small, and vanishes in the high doping limit.

In Fig. 7.8a the reduced dominance of thermal fluctuations with doping is clearly captured by the decrease in $Gi$. Its dependence on anisotropy is closer to the 3D $1/\varepsilon^2$ than to the 2D $\varepsilon$-independent behavior. Remarkably, the disorder amplitude in Fig. 7.8b also decreases with doping. This contrasts the result of Ref. [57], which found that oxygen addition increases the defects concentration. The apparent contradiction is resolved by noting that the disorder amplitude is affected also by the anisotropy dependence of the effective pinning potential, which decreases with doping as the vortex stacks get stiffer. The overall decrease of $R$ suggests that the latter mechanism is dominant, not the rising defect concentration.

Last, while both $Gi$ and $R$ decrease with doping, $Gi$ has a stronger dependence on anisotropy. This clarifies the true mechanism that shifts the maximum of the FO line and its bisection with the SO line towards higher temperatures with doping (Fig. 7.6). Although the magnitude of the disorder amplitude decreases with increased doping, disorder still gains *relative* dominance over thermal fluctuations, which decrease faster with $\varepsilon$.

## 7.3 The Effect of Columnar Defects on the Properties of $NbSe_2$ in the Vicinity of the Peak Effect

Here we study the effect of columnar defects on the dynamic behavior of vortices in the vicinity of the peak effect. This study was motivated by the notion that columnar defects may cause the metastable disordered states in the vicinity of the peak effect to disentangle, rendering the peak effect sharp. Our findings suggest a qualitatively different effect.

We measured three $NbSe_2$ samples with columnar defects of matching fields $B_\phi = 5, 10, 20$G and two samples of $B_\phi = 40$G ($B_\phi = n\phi_0$ where $n$ is the density of columns and $\phi_0$ is the flux quantum). The effect that will be described below was pronounced in two samples of matching fields $B_\phi = 5, 40$G. Two other samples with matching fields $B_\phi = 20, 40$G displayed a mild effect and the sample with $B_\phi = 10$G showed no effect at all.

Within this study, we performed several types of measurements. The results of these measurements differ from our expectations, as will be described

in detail later. Presented here are these intriguing results of which our understanding remains incomplete. Further experiments within this study may cast light on the remaining open questions. It should be noted, however, that only two of the five measured samples displayed a pronounced effect. Thus, other scenarios which may not rely on the effect of columnar defects on metastable states can not be ruled out. Presented in this report are results of three kinds of measurements:

1. Measurements of the ac critical current at various frequencies as a function of the external magnetic field, performed simultaneously on the pristine and the irradiated sides. In two of the samples, the results of these measurements illustrate a pronounced effect of the columnar defects on the frequency dependence of the critical current in the vicinity of the peak effect. Surprisingly, columnar defects seem to enhance the disordered metastable state in the sample, contrary to our expectation. A more detailed examination of the relevant length-scales involved led us to suspect that the disordered metastable states present in the irradiated sample may originate from the bulk of the sample rather than from edge contamination.

2. Measurements of the ac response in presence of a small dc bias were performed in order to check the possibility of a bulk-related mechanism which creates disordered metastable states in the bulk of a sample with columnar defects. The results of these measurements indicate that disordered metastable states may also be created in the bulk of these samples. Nevertheless, edge contamination was found to be an important ingredient in the effect of columnar defects on the amount of disordered metastable states in irradiated samples.

3. Next, we wanted to check whether our findings are indeed due to the effect of columnar defects on disordered metastable states in the sample. We repeated the measurements of section (1) in an external magnetic field tilted by $\theta = 45°$. In a tilted field, the frequency dependence of the critical current remained substantial, which suggests that something other than columnar defects may be causing the dramatic difference between our measurements on the pristine and the irradiated sides. However, evidence that support the scenario according to which it is the columnar defects that cause the enhancement of disordered metastable states seem to be convincing too. Thus, summing up our findings, the question what causes the enhanced frequency dependence in the vicinity of the peak effect in an irradiated sample remains open. It may

be worth to proceed with this study in order to answer the intriguing questions it raises.

Details of these experiments are presented below:

1. In this measurement session we measured the critical current as a function of the external magnetic field in the vicinity of the order-disorder transition. We compared results between the irradiated and the pristine halves of each sample. Assuming that columnar defects would disentangle the metastable disordered states, we expected that they would cause the peak in the critical current to drop more sharply. Based on the same assumption we also expected columnar defects to reduce the field-range of frequency dependence of the critical current. The result was contrary to that. The drop of the peak became smoother and the field-range of frequency dependence of the critical current became wider. These findings can be explained by enhancement of the disordered metastable states by the columnar defects.

   In order to measure the critical current, we have performed V(I) measurements on the pristine and the irradiated side of each sample simultaneously in a constant external magnetic field between 0 and 1T at temperature T=4.2K. Presented in figure (7.9a) are the critical currents of side 1-irradiated (red) and side 2-pristine (blue) of the sample with $B_\phi = 5$G at T=4.2K as a function of the external magnetic field at frequencies 3.3Hz (solid line), 33Hz (dashed line), 121Hz (dashed-dotted line) and 328Hz (dotted line).

   In the disordered phase, just below $H_{c_2}$ the critical current is not affected by columnar defects and measurements of the two sides of the sample look similar, as expected.

   In the ordered phase below the peak, on the pristine side the results matched our expectations. The drop of the critical current is wide and is frequency dependant [67] between $H \sim 0.82$T and $H \sim 0.92$T. In this field range metastable disordered states of high critical current occupy a considerable fraction of the sample. These states are injected through the edges of the sample. As frequencies are increased, a narrower strip on either side of the sample is accommodated by them, and their relative weight in the total critical current is lower.

   On the irradiated side, columnar defects modify the behavior of the critical current significantly in the ordered phase. However, this change is different than the one we expected. Contrary to our expectations, the peak on the irradiated side is even wider and its drop is smoother.

In addition, the frequency dependence is spanned on a larger field range and persists down to $H \sim 0.2$T. This result is surprising. We expected columnar defects to stretch the entangled vortices of the metastable-disordered states and assist their annealing. The result of this would be a sharper drop of the peak in the critical current and a smaller field range of frequency dependence. In reality, however, it seems that columnar defects do the opposite. They allow the metastable states to exist in the sample at low fields far from the transition, where, in a pristine sample, their lifetime is practically zero. This finding is further intriguing in its magnitude: e.g. at a field of 0.7T, with a matching field of $B_\phi = 5$G, we have 1400 vortices per columnar defect. Such a substantial change in the critical current by a small density of columnar

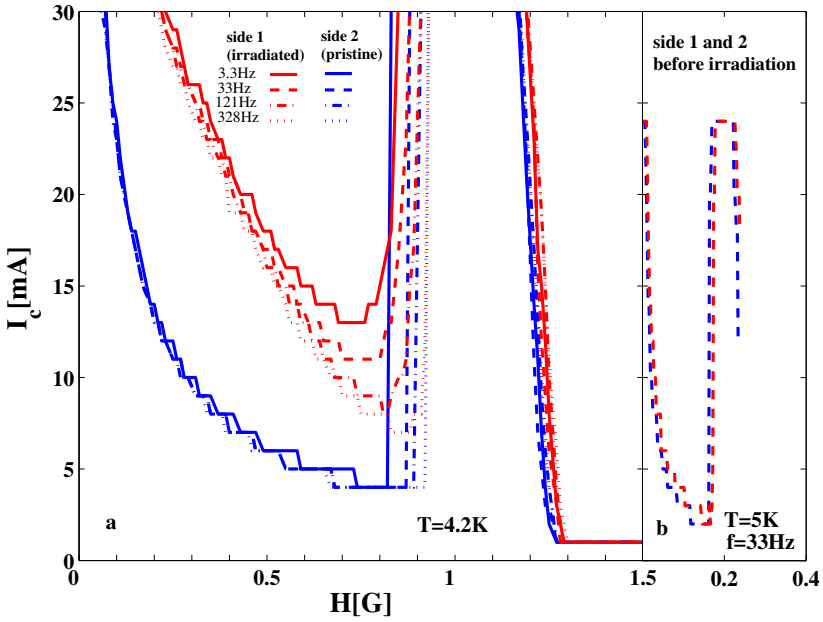


*Fig. 7.9:* Critical current as a function of the external magnetic field on side 1-irradiated (red) and side 2-pristine (blue) of the sample with $B_\phi = 5$G. (a) After irradiation. Measurements were conducted at T=4.2K with ac currents of frequencies 3.3Hz (solid line), 33Hz (dashed line), 121Hz (dashed-dotted line) and 328Hz (dotted line). There is a pronounced difference between the frequency dependence at fields below the peak effect (below 0.8T) on the pristine and irradiated sides. (b) Before irradiation, on side 1 (red) and side 2 (blue) of that sample. This was a control measurement which shows that the two sides of the sample behaved similarly before the irradiation. It was conducted at T=5K and f=33Hz.

defects was not anticipated. It may imply that some kind of a collective mechanism is involved.

In order to ensure that our findings are a result of the irradiation, and not an asymmetry in the sample, we performed a control measurement before the irradiation. Figure (7.9b) shows the critical currents as a function of the external magnetic field on side 1 (red) and side 2 (blue) of that sample before irradiation at $T = 5$K and $f = 33$Hz. The measurements of the two sides of the sample are almost identical throughout the measured field range. In particular, their critical currents in the ordered phase at fields below the peak effect (0.2T) show no significant difference. This illustrates that the sample was symmetric in terms of edge contamination before columnar defects were introduced to it, suggesting that the pronounced asymmetry between the irradiated and the pristine sides which is presented in figure (7.9a) is indeed caused by the columnar defects. Unfortunately, we did not measure the frequency dependence of the critical current in the control session, an experiment which could have proved this point beyond doubt.

After irradiation, we performed similar measurements in higher frequencies in order to reach saturation in the frequency dependence, on the irradiated side of the sample. We were surprised to find that saturation was obtained only at $f \sim 1$KHz. This is double the pristine saturation frequency, $f \sim 500$Hz. At such a high frequency only thin strips on either sides of the sample can be covered with edge-originated metastable disordered states. Thus, frequency dependence of the critical current at high frequencies may imply that metastable disordered states are created by the columnar defects in the bulk.

2. The result of measurement session 1 suggested that in presence of columnar defects disordered metastable states may be created in the bulk in addition to being injected from the edges. In measurement session 2 we wanted to examine this possibility. Therefore, we measured the ac response, $R_{ac}$, in presence of a small dc bias. In a pristine sample, the ac response is extremely sensitive to a small dc bias. This is a natural consequence of the edge-contamination mechanism. At very small biases the disordered phase is present only within $L_f$ from the edges, as in the absence of a bias, where the disordered vortices leave and re-penetrate every cycle. However, as $I_{dc}$ is increased, the bulk of the sample becomes contaminated by the penetrating disordered vortex phase, leading to a marked drop of $R_{ac}$ [67].

   Figure 7.10 shows the ac response of the irradiated sample to a small

dc bias at $I_{ac} = 19$mA with frequency $f = 1333$Hz and $B = 0.82$T. A dc bias of only 15% to 20% suppresses $R_{ac}$. The inset shows the pristine (blue) and irradiated (red) ac response at zero dc bias. The pristine pure ac response is larger by an order of magnitude than the irradiated one as was already observed in the ac measurements.

In order to distinguish between edge and bulk mechanism scenarios we need to compare $L_f$, the forward displacement of vortices during a cycle, to relevant length scales in the sample. $L_f$ is given by

$$L_f \sim v/2f \sim 5\mu\text{m} \tag{7.1}$$

where $f = 1$KHz is the frequency and $v$ the vortex velocity, which can be estimated from the voltage, $V = 1\mu$V, taken from measurements in the absence of dc bias at a magnetic induction $B \sim 0.8$T by $v = V/Bl \sim 10^4\mu$m/s. Here, $l = 100\mu$m is the distance between voltage contacts.

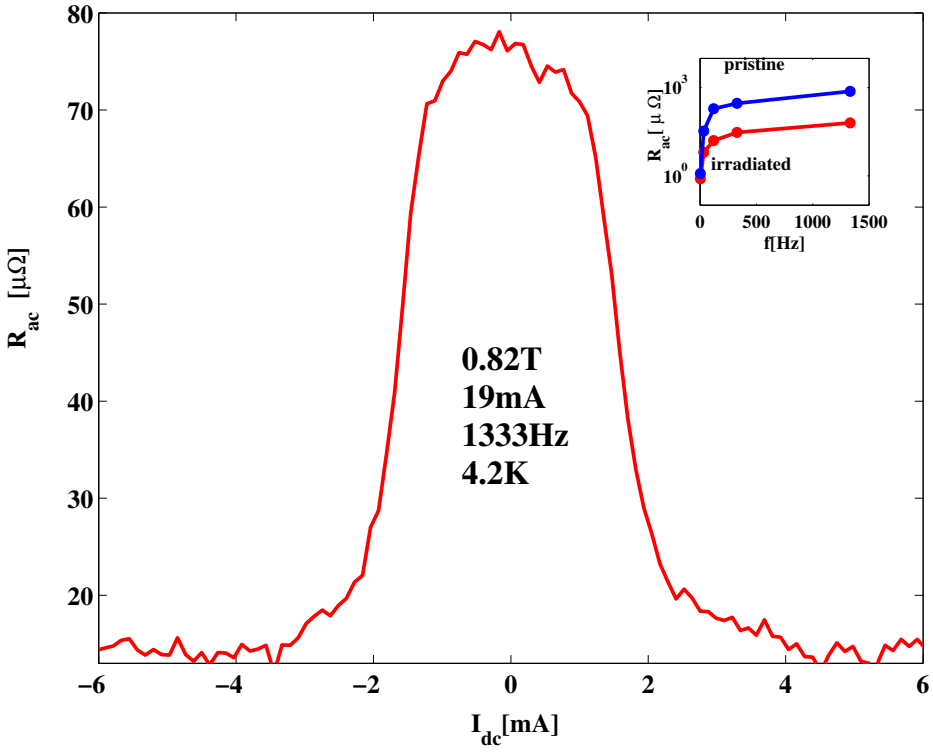


*Fig. 7.10:* The measured resistance as a function of dc bias in the irradiated side of the sample. Inset: a comparison between the zero-bias response of the pristine and irradiated sides of the sample.

From a comparison to the sample width, $w$, it seems that an edge-contamination mechanism can not be responsible alone for the enhancement of the disordered metastable states in the irradiated samples. If only an edge-related mechanism is involved, then $L_f$ at relevant frequencies must be comparable to this length scale. However, our sample width is $w = 600\mu$m, therefore $L_f : w \sim 1 : 120$. It implies that the relative weight of edge-originated disordered states in the critical current is small at $f = 1$KHz, suggesting that columnar defects may alter the critical current with a bulk related mechanism.

However, from a comparison of $L_f$ to the mean columnar defect separation, $L_{CD}$, it appears that a bulk-related mechanism also cannot be responsible alone for the enhancement of the disordered metastable states in the irradiated samples. If columnar defects *create* metastable disorder in vortex matter which passes by it, then disorder should be located around a distance $L_f$ from each columnar defect. At low frequencies at which $L_f > L_{CD}$ the whole sample is covered with disorder and the critical current is high. At higher frequencies, at which $L_f < L_{CD}$ disorder is located only in a small region around the columnar defects, and the critical current is low. In that case, a small dc bias can spread disorder over the sample and suppress the ac response to zero. The data in figure 7.10 suggests that the enhancement of edge-contamination by columnar defects is also significant. In our sample $B_\phi = 5$G which corresponds to $L_{CD} \sim 2\mu$m. At $f \sim 1$KHz we have $L_f \sim 5\mu$m$> L_{CD} \sim 2\mu$m which implies within a bulk mechanism scenario a disorder-covered sample. Nevertheless, we see that a small dc suppresses the ac response down to the noise level. These equivocal findings suggest that both edge and bulk mechanisms may affect the critical current. Further investigation is required in order to determine how the scenarios of the two mechanisms can be integrated

3. Concerned by the fact that only two of the five samples that we measured displayed a pronounced difference between the irradiated and the pristine sides, we wanted to check that this difference is indeed a result of the irradiation and not some other kind of asymmetry in the sample. Therefore, we performed ac V(I) measurements with the external magnetic field tilted by $\theta = 45°$. Presented in figure 7.11 are the critical currents of the irradiated (red) and pristine (blue) sides of the sample with $B_\phi = 5$G at T=4.2K as a function of the external magnetic field tilted at (a) $\theta = 45°$ (b) $\theta = 0°$. Injected ac currents were at frequencies 3.3Hz (solid line), 33Hz (dashed line), 121Hz (dashed-dotted line) and 328Hz (dotted line). We expected that an angle between the vortices

and the columnar defects would suppress their effect on vortex matter and on the critical current, yielding a similar frequency dependence on the pristine and irradiated sides. Surprisingly, we found that the frequency dependence of the critical current on the irradiated side remained qualitatively similar to this dependence with field at $\theta = 0°$. Since a mechanism in which columnar defects entangle vortices involves

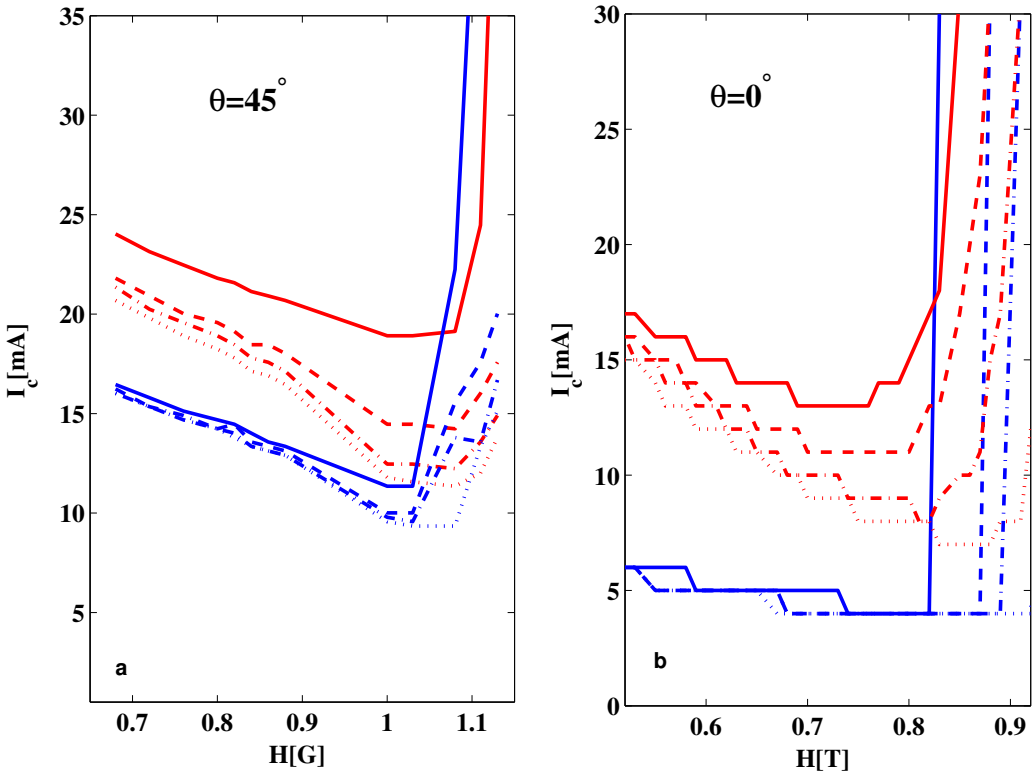


*Fig. 7.11:* Critical current of the irradiated (red) and pristine (blue) sides as a function of the external magnetic field tilted at (a) $\theta = 45°$ (b) $\theta = 0°$ with respect to the dirrection of the columnar defects with $B_\phi = 5G$. Measurements were performed at T=4.2K with ac currents of frequencies 3.3Hz (solid line), 33Hz (dashed line), 121Hz (dashed-dotted line) and 328Hz (dotted line)

pinning of only vortex fragments to columnar defects, it may be reasonable to assume that this mechanism continues to be effective in presence of a tilted magnetic field, depending on the elasticity of the vortices and on the pinning potential of the columnar defects.

The three experiments that were presented here bring the main results of

this study. They leave the intriguing question of how columnar defects affect vortex matter in the vicinity of the peak effect open. Further investigation is required in order to resolve this issue.

## 7.4 Surface Superconductivity in $MgB_2$

Motivated by evidence which suggest that its resistive transition broadening originates in a surface related mechanism [76, 77, 78, 79] we studied $MgB_2$ focusing on the physics of the surface using the self field measurement approach [90].

We performed various measurements, Some of these measurements will be described in the following. Summing up our findings, we conclude that very large signals that result from ac heating of the samples by transport current obscure our real data.

The results presented here were obtained using two single crystals of $MgB_2$ [104, 105, 106], A and B. The dimensions of sample A were $100X80X50\mu m^3$ whereas those of sample B were $270X135X50\mu m^3$. Their critical temperature was $T_c \approx 37K$. Crystals A and B has two and four electric contacts respectively (see figure 5.4b and d) in order to allow self-field measurements.

Presented in this section are results of the following measurements:

1. Measurements of the self field induced by an ac current while sweeping the temperature from above $T_c$ at various constant external magnetic fields applied to sample A. From these measurements we find that indeed, the current pattern varies from a typical evenly distributed pattern above $T_{onset}$ to current which flows mostly on the edges of the sample. However, the obtained distribution of the self field did not display a complete sign inversion as expected. This may indicate an intrinsic or geometric asymmetry of the sample.

2. The following two types of asymmetric measurements of a self induced field were performed on a second sample, B. These were motivated by the notion that introducing a symmetry breaker in the driven current could compensate for the possible geometric or material asymmetry of the sample and result in the expected even distribution of current between the edges below $T_{onset}$.

   **a.** Measurements of the self field induced by ac current in the presence of an additional large dc current during a sweep of the temperature from above $T_c$.

   **b.** Measurements of the self field induced by a square ac current which alternates between 0 and $I$ while sweeping $I$ from -40mA to 40mA.

Inverse Biot-Savart transformations of the data obtained in these experiments revealed that in a wide field and temperature range the current flows in a paramagnetic loop-like pattern. This observation was also supported by the results of similar experiments we performed in the presence of an inverted magnetic field.

3. In order to verify our suspicion that most of the self-field signal we measured originates in ac heating of the sample, we measured the self-field induced by ac current driven in sample B at various frequencies. Indeed, the resulting frequency dependence of the signal confirmed our suspicion.

Details of these experiments are presented below:

1. In order to determine where the current flows, we scanned the temperature from 50K to 6K and performed self field measurements on $MgB_2$ crystals using ac currents of amplitudes 0.5mA to 30mA. These experiments were performed in the presence of a constant external magnetic field in the range 0.005T-1T. Presented in figure 7.12 is a typical result of a self field profile $B_{ac}$ measured by Hall-sensors 2 to 5 (see inset for their location compared to the sample) of sample A, as a function of the temperature. The signal was generated by an ac current of amplitude 30mA. An external dc magnetic field of $H_{dc} = 0.15T$ was applied during the experiment.

   Above $T_{onset}$, between 37K and 50K the current flows uniformly across the sample, as expected. Accordingly, the $B_{ac}$ distribution is similar to that in figure 5.2a with a monotonic decrease in the amplitude from sensor 2 to sensor 5 as the center of the sample is approached from its edge. Below $T_{onset}$ the positive self-field signal of these sensors, which are all located on one side of the sample, drops to a lower value. This drop is expected when the current changes from a uniform flow to an edge-only flow. However, the signal did not exhibit a sign inversion as it should in this case (see figure 5.2b). From that we deduced that an intrinsic or a geometric asymmetry of the sample may be preventing a complete sign inversion of the signal.

2. In order to compensate for the asymmetry which we found in most crystals, we performed the following two asymmetric self-field experiments on a second crystal, B.

   **a.** We scanned the temperature from above $T_c$ and measured the field induced by a small (3mA) ac current while driving a large dc current

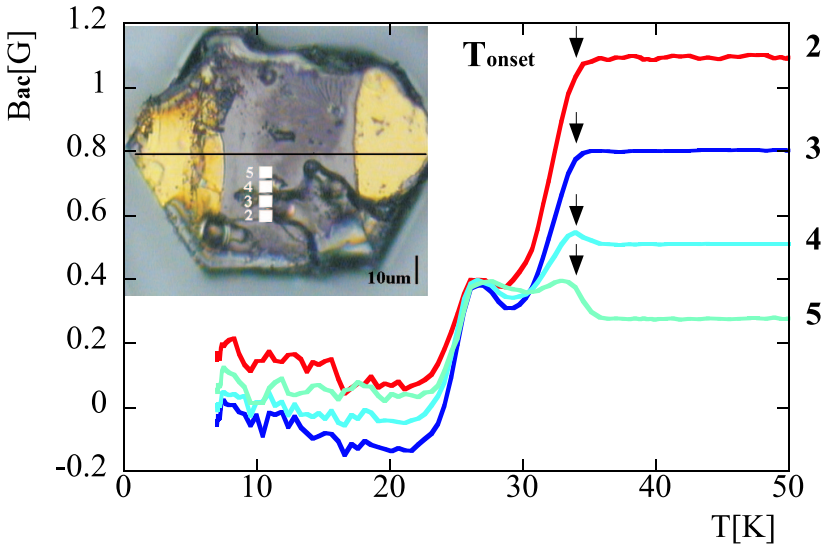


*Fig. 7.12:* The self induced field $B_{ac}$ at sensors 2-5 (see inset for their location) generated by an ac current of amplitude 30mA driven in an $MgB_2$ crystal A, in the presence of an external magnetic field $H_{dc} = 0.15T$ as a function of the temperature while cooling from above $T_c$. At elevated temperatures the current flows uniformly across the sample. Below $T_{onset}$ the self field signal drops dramatically indicating that more of the current flows along the edges. The inset shows $MgB_2$ crystal A with the location of sensors 2-5 indicated by the white squares.

in the sample. The dc current, which played the role of a symmetry breaker in the experiment, varied between -40mA and 40mA. The experiment was performed in a constant external dc field between 50G and 1500G.

In this sample sensors 1 and 2 do not reside underneath the sample, sensor 4 is located under the edge of the sample, sensor 13 is located roughly under its center, whereas sensors 14-17 reside beyond its center, towards its opposite edge. A typical self field signal $B_{ac}$ measured by sensors 1-17 in a constant field of $H_{dc}$ =50Oe with a dc current of 40mA is shown in figure 7.13a. The self field profile in this measurement does not match the expected profile induced by transport current flowing

only on the edges of the sample. In particular, in the temperature range between 26K and 31K an exceptionally large value of the self field signal stands out. It reaches a value of 0.8G in its peak. This is markedly large as compared to the signal above $T_{onset}$ which does not exceed 0.02G. In figure 7.13b the signal of a single sensor (number 7) is presented at various applied dc currents. Here, a shift in the peak's onset temperature, $T_{onset}$, is observed as the dc current is raised. This finding had hinted, at this early point, the possible existence of a heating problem. However, dc heating can not explain the shape and size of the signal in this measurement.

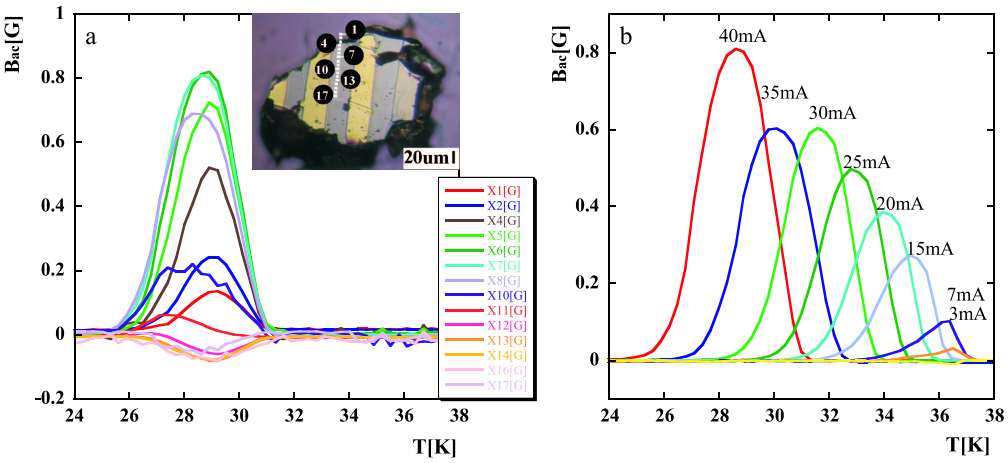


*Fig. 7.13:* (a) A self field signal $B_{ac}$ resulting from ac current of 3mA, picked up at sensors 1-17 of sample B (see inset for an image) as a function of temperature, at a constant magnetic field H=50Oe in presence of a dc current $I_{dc}$ = 40mA. (b) The $B_{ac}$ signal in sensor number 7 of sample B, which is located about half way between the sample's center and one of its edges, for various dc currents of magnitude 3mA to 40mA. The inset shows an image of sample B with sensors 1-17 marked by the small white squares.

**b.** We measured the field induced by a square ac current alternating between 0 and $I$, while varying $I$ from -40mA to 40mA. This experiment was performed in a constant external magnetic field in the range 0.005T-0.07T and a constant temperature in the range 28K-40K.

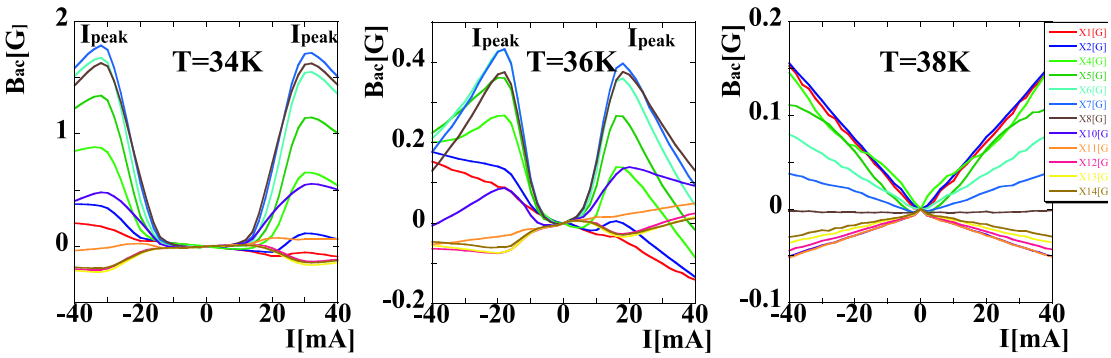


*Fig. 7.14:* A self field measurement in sensors 1-14 (skipping 3,9) of sample B with a square current varying between 0 and I, while I is varied between -40mA and 40mA. These measurements were taken at a constant external temperature of T=34K(a), T=36K(b) and above $T_c$ at T=38K(c). A peak in the signal appears at $I_{peak}$ = 30mA and $I_{peak}$ = 18mA in temperature of T=34K and T=36K respectively. At T=38K there is no peak in the signal.

Presented in figure 7.14 is the self field signal of a square current at temperatures (a) T=34K, (b) T=36K and (c) above $T_c$ at T=38K in a constant external magnetic field $H_{dc}$ = 50Oe. At temperatures T=34K and T=36K as the amplitude of the current is increased from 0 to $I_{peak}$, the $B_{ac}$ signal at most of the sensors increases gradually until at $I_{peak}$ it starts dropping again. At T=34K $I_{peak}$ ≃30mA. As the temperature is increased, $I_{peak}$ decreases until it reaches a value of $I_{peak}$ = 18mA at T=36K and then at T=38K it disappears altogether.

We performed an inverse Biot-Savart transformation from the $B_{ac}$ distribution to the current distribution in the sample using a matlab program. This program searches for the current distribution and values of the unknown geometrical parameters which produce the best fit for our measured field distribution. First, the self field signal of an evenly distributed current (measured above $T_c$) is subtracted from the measured $B_{ac}$. Next, relying on the resemblance of our measured ac field distribution to that induced by a loop of current, it assumes that the measured ac field is a result of current flowing in two wires parallel to the edges of the sample. It then searches for the best fit for a vertical and horizontal location of these wires and for the value of the response

currents in them.

The result of a typical fit are presented in figure 7.15a. The values of the self induced field $B_{ac}$ measured by sensors 4 to 17 at T=36K in an external field of H=50Oe while driving a square ac current of 40mA are marked by dark blue diamonds ($\diamondsuit$) as a function of the sensors' location. The dark blue line connecting between these measured data points is a guide to the eye. The solid light blue line presents a fit to the measured $B_{ac}$ distribution. Note that the fit distribution is in a very good agreement with the measured one within the sample. Our program found that the following parameters produce the best fit to the measured data: an ac current of 3.4mA in the left wire located $40\mu m$ horizontally away from our origin and an ac current of -3.4mA in the right wire at a horizontal distance of $150\mu m$ from this origin. The calculated location of the wires is marked in figure 7.15a by solid red circles ($\bullet$). The calculated vertical distance of these wires from the sensors is $50\mu m$. These geometric parameters agree well with our estimates of the crystal's thickness and the location of the sensors.

These results, presents in figure 7.15a were calculated to fit a single measured data point from a current sweep experiment. Similar calculations were performed to obtain the distribution of the response ac current and geometrical parameters throughout the experiment. The results as a function of the magnitude of the applied current are presented in figure 7.15b. It shows the evolution of the response currents in the left (solid red circles) and right (open blue circles) wires as the applied current was varied from -40mA to 40mA at T=36K and $H_{dc} = 50$Oe. The solid lines are guide to the eye. As the transport current is introduced initially, the sample responds in a paramagnetic loop of current. As the amplitude of the applied current is further increased, the amplitude of the calculated response current loop increases too, and continues to increase until the transport current reaches 20mA. From this point on, the increase of the transport current is responded by a decrease of the loop current. Notice that the direction of the flow of current in the loop remains the same for both directions of the transport current. Presented in figure 7.15c is the fit for the geometric parameters from this measurement. These fit parameters obtained from each data point in the experiment independently remain at an almost constant value throughout the measurement and are in good agreement with our estimates of the geometric parameters of the sample.

It seems that driving transport current causes the sample to respond by an increasing loop of current in order to produce a paramagnetic

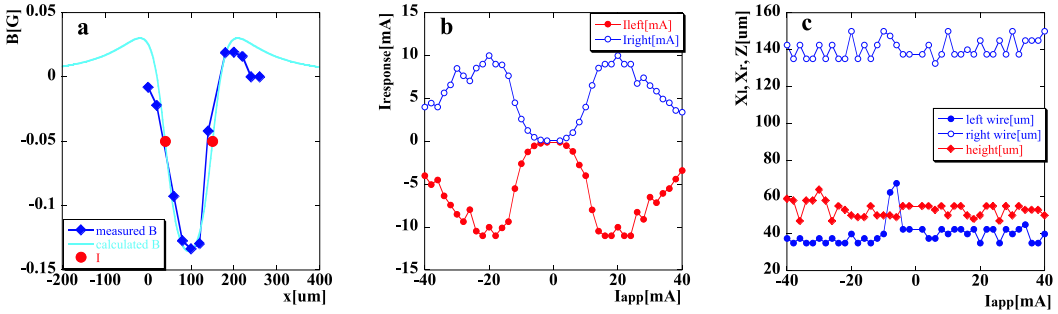


*Fig. 7.15:* (a)The values of the self-induced field $B_{ac}$ measured by sensors 4-17 of sample B, at $T = 36$K in an external field of $H_{dc} = 50$Oe while driving a square ac current of 40mA are marked by dark blue diamonds ($\diamondsuit$) as a function of the sensors' horizontal location according to our estimates. The dark blue line connecting between these measured data points is a guide to the eye. The solid light blue line presents a fit to the measured $B_{ac}$ distribution. The calculated location of the current wires is marked by solid red circles ($\bullet$). (b) The currents in the left (red solid circles) and right (blue open circles) wires used in the fit for the full current sweep from -40mA to 40mA at $T = 36$K and $H = 50$Oe shown in figure 7.14. The solid lines are guide to the eye. (c) The geometric parameters calculated for each data point in this measurement as a function of the applied current $I_{app}$. The calculated horizontal location of the left and right wires is marked in blue solid and open circles whereas their calculated vertical height above the sensors is marked in red solid diamonds ($\diamondsuit$). The solid lines are guide to the eye.

response. This observation is also supported by the results of similar experiments we performed in the presence of an inverted external magnetic field. Relying on these results and on the fact that the equilibrium magnetization of a superconducting sample depends on its temperature we conclude that the source of this paramagnetic response is ac heating of the sample by the applied ac current.

The ac asymmetric square current causes a modulation of the sample's temperature, the sample then modulates its magnetization by a modulation of its screening current. It is the self field signal induced by this modulated screening current that we measured (in addition to a self-field generated by a uniform current of amplitude $I_{app}$ that we

have subtracted from the data). The magnetic induction of a superconducting sample increases monotonically with temperature, and in our sample also with the applied transport current. The resulting signal is that of a paramagnetic response.

This explanation is consistent with all of our previous findings: Since the heating mechanism does not distinguish between positive and negative current, we measured an identical signal for applied currents of inverted signs, as seen in figure 7.15b. It also agrees with the inverted sign of signals that we got for an inverted field experiment, as expected from a paramagnetic response. The peaks in the measured signal observed at $I_{peak}$ in figures 7.14a and 7.14b can be explained by a competition between two trends as the magnitude of the applied current is increased. The measured self field ac signal is proportional to $\partial M/\partial T \Delta T$. On one hand, as the applied current is increased, the amplitude of the temperature modulation $\Delta T$ increases too. The derivative of the magnetization $\partial M/\partial T$, on the other hand, decreases as the temperature is increased from $T_{c1}$ where its value is maximal towards $T_{c2}$ where the magnetization becomes nearly independent of temperature and $\partial M/\partial T$ is close to zero.

3. In order to further verify our conclusion, we measured the frequency dependence of the self-field signal. As the temperature of the sample has a finite response time to variations of heat caused by the alternating current, the amplitude of the temperature modulation depends on the frequency of the current. At a low frequency, the slow varying current can be followed by an appropriate temperature modulation, whereas at a high frequency the temperature modulation can only follow partially and its amplitude is thus reduced. As a result, a self-field signal which originates in ac heating should increase as the frequency of the applied current decreases. Presented in figure 7.16 are the self-field signal induced by ac current at frequencies $f$=33Hz (solid red line), $f$=283Hz (dashed dark blue line), and $f$=586 (dotted light blue line) and measured by sensor 7 of sample B, in the presence of an external magnetic field $H_{dc}$ = 50Oe and a dc current $I_{dc}$ = 20mA. Indeed, the self-field signal increases as the frequency of the current by which it was induced is decreased, as expected within the scenario of ac heating.

Summing up the findings discussed above, we conclude that a large part of the signal that we measured in our experiments was due to ac heating in the sample. This artifact obscured the physically interesting data that we were interested in. In order to be able to measure that physical data the

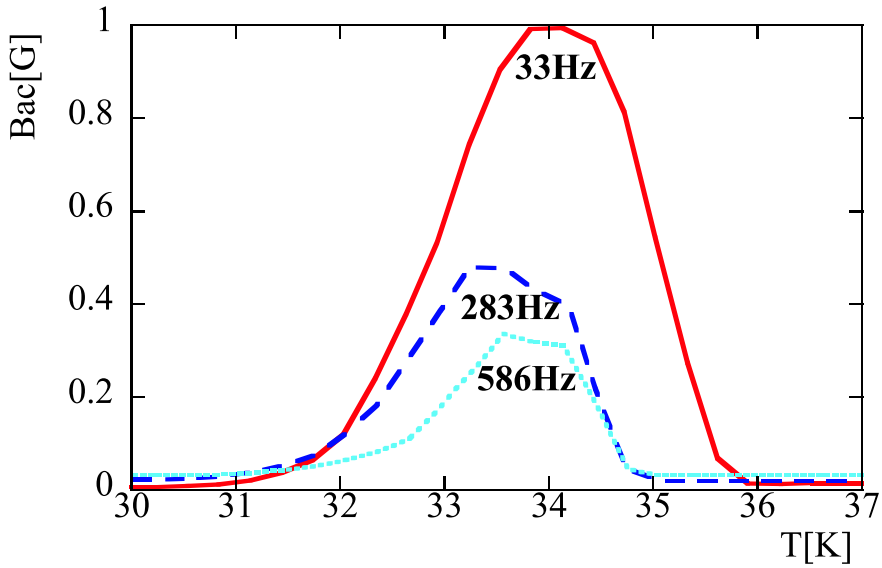


*Fig. 7.16:* Frequency dependence of the self-field signal, induced by ac current at frequencies $f$=33Hz (solid red line), $f$=283Hz (dashed dark blue line), and $f$=586 (dotted light blue line) and measured by sensor 7 of sample B, in the presence of an external magnetic field $H_{dc}$ = 50Oe and a dc current $I_{dc}$ = 20mA. The signal increases with the decrease in the frequency.

heating problem must be addressed. This can be done by several means. The obvious way is to improve the resistance of the electric contacts. Another way is to use thinner samples with a large and flat face to obtain a better thermal contact with the underlying GaAs chips.

# 8. SUMMARY

In section 7.1, we presented thermodynamic evidence for new first-order - second-order - first-order behavior of the melting line in BSCCO samples irradiated with a low density of columnar defects. This unusual behavior is due to close competition between four different energy scales in the dilute columnar defects limit. As columnar defects are introduced, the melting transition initially alters its order from first to second at intermediate temperatures where correlated pinning has a dominant effect. At high and low temperatures the transition remains first-order despite the disordering potential of columnar defects. At low temperatures where the melting field is high, the solid phase is dominated by elasticity rather than correlated pinning due to the increasing number of vortices per columnar defects, and the first-order transition is retained. The first-order nature of the transition is likewise preserved at high temperatures, where correlated pinning is weakened by thermal fluctuations. As the density of the columnar defects is increased, the second-order segment of the transition line expands both to the higher and lower temperatures. In one sample a second-order transition was also found on the low-temperature side of the inverse melting portion, resulting in an even more complex first-order - second-order - first-order - second-order sequence. The observed nucleation and growth process of the second-order segments along the original first-order transition line clarifies the general process of transformation of phase transitions with increased disorder. In particular, it describes the mechanism that leads to transformation of a Bragg glass in the presence of point disorder to a BoG at high concentrations of correlated disorder, which melts through a single second-order transition.

In section 7.2, we showed that anisotropic scaling accounts for the reduced anisotropy of BSCCO samples with doping down to a temperature $t_{\rm th}$. Below $t_{\rm th}$, where disorder becomes relevant, the anisotropic scaling still collapses the second-order transition lines. We found that disorder and thermal-fluctuations weaken relative to elasticity with increased doping, which shifts the first-order melting line towards higher fields. Disorder still gains relative dominance over thermal fluctuations, which concurrently shifts the maximum of the first-order line and its bisection with the second-order line towards

higher temperatures.

In section 7.3 we presented evidence which suggest that the disordered metastable states near the peak effect of the critical current in $NbSe_2$ are enhanced by the presence of columnar defects. Whether this enhancement occurs predominantly at the edges of the sample and is linked to the edge contamination mechanism or in the bulk of the sample remains an open question for future investigation.

# 9. BIBLIOGRAPHY

# BIBLIOGRAPHY


[1] Yoseph Imry and Michael Wortis, Phys. Rev. B **19**, 3580 (1979).

[2] D.S. Fisher, M.P.A. Fisher and D.A.Huse, Phys. Rev. B **43**, 130 (1991).

[3] V.L. Ginzburg and L.D. Landau, Zh. Eksp. Teor. Fix, **20**, 1064 (1950).

[4] G. Blatter, V.B. Geshkenbein, and A.I. Larkin, Phys. Rev. Lett. **68**, 875 (1992).

[5] U. Essman, H. Träuble, *Phys. Lett*, **24A**, 526 (1967).

[6] D. Criber, B. Jarcot, L. Mdhav, B. Farnoux, *Phys. Lett*, **9**, 106 (1968).

[7] H.W. Weber, J. Scheller, G. Lippman, *Phys. Status Solidi (b)*, **57**, 515 (1973).

[8] M. Koyanagi, R.P. Huebener, J. Bosch, R. Gross, *Phys. Rev. Lett.*, **54**, 1448 (1985).

[9] T. Matsuda *et al.*, *Phys. Rev. Lett.*, **62**, 2519 (1989).

[10] P.H. Kes, A.M. Troyanovski, J. Aarts, Nature **399**, 665 (1999).

[11] A.M. Change *et al.*, *Europhys. Lett.* **20**, 645 (1992).

[12] P.E. Goa *et al.*, *Supercond. Sci. Technol.* **14**, 729 (2001).

[13] G. Blatter and V.B. Geshkenbein, *The Physics of Superconductors* (Springer, New York, 2003).

[14] E.H. Brandt, *Phil. Mag. B* **80**, 835 (2000).

[15] D.R. Nelson, Phys. Rev. Lett. **60**, 1973 (1988).

[16] E. Zeldov *et al.*, Nature **375**, 373 (1995).

[17] H. Safar *et al.* Phys. Rev. Lett. **69**, 824 (1992).

[18] D.T. Fuchs *et al.*, Phys. Rev. B **54**, R796 (1996).

[19] H. Pastoriza *et al.* Phys. Rev. Lett. **72**, 2951 (1994).

[20] R.A. Doyle *et al.* Phys. Rev. Lett. **75**, 4520 (1995).

[21] A. Schilling *et al.*, Nature **382**, 791 (1996).

[22] R. Cubitt *et al.*, Nature **365**, 407 (1993).

[23] S.L. Lee *et al.* Phys. Rev. Lett. **71**, 3862 (1993).

[24] A.I. Larkin, *JETP* **31**, 784 (1970).

[25] A.I. Larkin and Y.N. Ovchinnikov, *Journal of Low Temperature Physics* **34**, 409 (1978).

[26] T. Giamarchi and P. LeDoussal, Phys. Rev. B **52**, 1242 (1995).

[27] T. Nattermann, Phys. Rev. Lett. **64**, 2454 (1990).

[28] T. Emig, S. Bogner and T. Nattermann, *Phys. Rev. Lett.* **83**, 400 (1999).

[29] T. Giamarchi and P. LeDoussal, Phys. Rev. B **55**, 6577 (1997).

[30] D. Ertas and D.R. Nelson, Physica C **272**, 79 (1996).

[31] J. Kierfeld, T. Nattermann and T. Hwa, Phys. Rev. B **55**, 626 (1997).

[32] A.E. Koshelev and V.M. Vinokur, Phys. Rev. B **57**, 8026 (1998).

[33] G.P. Mikitik and E.H. Brandt, Phys. Rev. B **64**, 184514 (2001).

[34] D. Li and B. Rosenstein, Phys. Rev. Lett. **90**, 167004 (2003).

[35] N. Avraham *et al.*, Nature **411**, 451 (2001).

[36] G.P. Mikitik and E.H. Brandt, Phys. Rev. B **68**, 054509 (2003).

[37] P. Olsson and S. Teitel, Phys. Rev. Lett. **87**, 137001 (2001).

[38] M.V. Feigelman and V.M. Vinokur, Phys. Rev. B **41**, 8986 (1990).

[39] H. Beidenkopf *et al.*, Phys. Rev. Lett. **95**, 257004 (2005).

[40] D. Li, B. Rosenstein, and V. Vinokur, J. Supercond. Novel Mag. **19**, 369 (2006).

[41] B. Khaykovich *et al.*, Phys. Rev. B **56**, R517 (1997).

[42] D.R. Nelson and V.M. Vinokur, Phys. Rev. Lett. **68**, 2398 (1992).

[43] M.P.A. Fisher, P.B. Weichman, G. Grinstein and D.S. Fisher, Phys. Rev. B **40**, 546 (1989).

[44] C.J. van der Beek *et al.*, Phys. Rev. Lett. **86**, 5136 (2001).

[45] L. Radzihovsky, Phys. Rev. Lett. **74**, 4923 (1995).

[46] A.I. Larkin and V.M. Vinokur, Phys. Rev. Lett. **75**, 4666 (1995).

[47] S. Tyagi *et al.*, Phys. Rev. B **67**, 214501 (2003) .

[48] C. Dasgupta *et al.*, Phys. Rev. B **72**, 94501 (2005).

[49] S.S.Banerjee *et al.*, Phys. Rev. Lett. **90**, 87004 (2003);

[50] S.S. Banerjee *et al.*, Phys. Rev. Lett. **93**, 097002-1 (2004).

[51] B. Khaykovich *et al.*, Phys. Rev. B **57**, 14088 (1998);B. Khaykovich *et al.*, Physica C **282**, 2068 (1997).

[52] M. Menghini *et al.*, Phys. Rev. Lett. **90**, 147001 (2003).

[53] B. Khaykovich *et al.*, Phys. Rev. Lett. **76**, 2555 (1996).

[54] Y. Yamaguchi *et al.*, Phys. Rev. B **63**, 014504 (2000).

[55] T. Hanaguri *et al.* Physica C **256**, 111 (1996).

[56] G. Blatter, M.V. Feiglman, V.B. Geshkenbein, A.I. Larkin and V.M. Vinokur, *Rev. Mod. Phys.* **66**, 1125 (1994).

[57] T.W. Li *et al.*, Physica C **257**, 179 (1996).

[58] T.G. Berlincourt, R.R. Hake and D.H. Leslie, Phys. Rev. Lett. **6**, 671 (1961).

[59] P.H. Kes and C.C. Tsuei, Phys. Rev. B **28**, 5126 (1983).

[60] S. Battacharya and M.J. Higgins, Phys. Rev. Lett. **70**, 2617 (1993).

[61] K. Ghosh *et al.*, Phys. Rev. Lett. **76**, 4600 (1996).

[62] W. Henderson *et al.*, Phys. Rev. Lett. **77**, 2077 (1996).

[63] C. Tang *et al.*, *Europhysics Lett.* **35**, 597 (1996).

[64] P.L. Gammel *et al.*, Phys. Rev. Lett. **80**, 833 (1998).

[65] X.S. Ling *et al.*, Phys. Rev. Lett. **86**, 712 (2001).

[66] Y. Paltiel *et al.*, Phys. Rev. Lett. **85**, 3712 (2000).

[67] Y. Paltiel *et al.*, Nature **403**, 398 (2000).

[68] M.J.P. Gingras and D.A. Huse, Phys. Rev. B **53**, 15193 (1996).

[69] S.S. Banerjee *et al.*, Appl. Phys. Lett. **74**, 126 (1999).

[70] J. Nagamatsu *et al.*, Nature **410**, 63 (2001).

[71] C. Buzea *et al.*, Supercond. Sci. Technol. **14**, R115 (2001).

[72] P.C. Canfield *et al.*, Physica C **385**, 1 (2003).

[73] M. Angst *et al.*, cond-mat/0305048 v2 (2003).

[74] A.K. Pradhan *et al.*, Phys. Rev. B **65**, 144513 (2002).

[75] Y. Eltsev *et al.*, Phys. Rev B **65**, 140501 (2002).

[76] T. Matui *et al.*, cond-mat/0210358.

[77] U. Welp *et al.*, Phys. Rev B **67**, 012505 (2003).

[78] L. Lyard *et al.*, Phys. Rev B **66**, 180502 (2002).

[79] A.V. Sologubenko *et al.*, Phys. Rev B **65**, 180505 (2002).

[80] D. Saint-James and P. de Gennes, Phys. Lett. **7**, 306 (1963).

[81] J.P. Burger *et al.*, Solid State Communications **2**, 101 (1964).

[82] G. Deutscher, J. Phys. Chem. Solids **28**, 741 (1967).

[83] C.F. Hempstead *et al.*, Phys. Rev. Lett. **12**, 145 (1964).

[84] D.P. Sefaphim *et al.*, Phys. Rev. **116**, 606 (1959).

[85] J.I. Budnick, Phys. Rev. **119**, 1578 (1960).

[86] S.H. Autler *et al.*, Phys. Rev. Lett. **9**, 489 (1962).

[87] W.F. Druyvesteyn *et al.*, Rev. Mod. Phys. **36**, 58 (1964).

[88] C. P. Bean and J.D. Livingston, Phys. Rev. Lett. **12**, 14 (1964).

[89] Y. Paltiel *et al.*, Phys. Rev. B **58**, 14763 (1998).

[90] D. Fuchs *et al.*, Nature **391**, 373 (1998).

[91] D. Fuchs *et al.*, Phys. Rev. Lett. **80**, 4971 (1998).

[92] L. Burlachkov *et al.*, Phys. Rev. B **54**, 6750 (1996).

[93] F. Pardo *et al.*, Phys. Rev. Lett. **78**, 4633 (1996).

[94] U. Yaron *et al.*, Nature **376**, 753 (1995).

[95] M. Konczykowski *et al.*, Physica C **408**, 547 (2004).

[96] M. Willemin *et al.*, Phys. Rev. Lett. **81**, 4236 (1998).

[97] G.P. Mikitik and E.H. Brandt, Phys. Rev. B **69**, 134521 (2004); G.P. Mikitik and E.H. Brandt, Superconductor Scielnce and Technology **20**, 9 (2007)

[98] B. Hayani *et al.*, Phys. Rev. B **61**, 717 (2000).

[99] R.J. Drost *et al.*, Phys. Rev. B **58**, 615 (1998).

[100] N. Avraham *et al.*, Phys. Rev. Lett. **99**, 087001 (2007).

[101] D. Mayer, Ph.D. thesis Weizmann Institute of Science, Rehovot, Israel (1997).

[102] S. Ooi, T. Shibauchi, and T. Tamegai, Physica C **302**, 339 (1998).

[103] N. Motohira *et al.*, J. Ceram. Soc. Jpn. Int. Ed. **97**, 994 (1989).

[104] M.S. Kim. *et al.*, Phys. Rev. B **64**, 12511 (2001).

[105] C.U. Jung *et al.*, Physica C **353**, 162 (2001).

[106] C.U. Jung *et al.*, Appl.Phys. Lett. **78**, 4157 (2001).

[107] J. P. Rodriguez, Phys. Rev. B **70**, 224507 (2004).

[108] Y. Nonomura and X. Hu, Europhys. Lett. **65**, 533 (2004).

[109] S. Colson *et al.*, Phys. Rev. B **69**, 180510 (2004).

[110] A. Schilling *et al.*, Phys. Rev. Lett. **78**, 4833 (1997).

[111] F. Bouquet *et al.*, Nature **411**, 448 (2001).

[112] U.Welp *et al.*, Phys. Rev. Lett. **76**, 4809 (1996).

[113] W.K. Kwok *et al.*, Phys. Rev. Lett. **84**, 3706 (2000).

[114] T. Hanaguri *et al.*, Physica C **256**, 111 (1996).

[115] J. Kierfeld and V. Vinokur, Phys. Rev. B **69**, 024501 (2004).

[116] V. Vinokur *et al.*, Physica C **295**, 209 (1998).

[117] R.A. Klemm and J.R. Clem, Phys. Rev. B **21**, 1868 (1980).

[118] L.I. Glazman and A.E. Koshelev, Phys. Rev. B **43**, 2835 (1991).

[119] L.L. Daemen *et al.*, Phys. Rev. Lett. **70**, 1167 (1993).

[120] M. Tokunaga *et al.*, Phys. Rev. B **67**, 134501 (2003).

[121] G.C. Kim *et al.*, Phys. Rev. B **72**, 064525 (2005).

[122] A.I. Larkin, and A. Varlamov. *Theory of fluctuations in superconductors* (Oxford, England, 2005), Chap. 2.